REVIEW

Check for updates

Decoding eumelanin's spin label signature: a comprehensive EPR analysis

João V. Paulin, [ID] *[a] Carlos F. O. Graeff [ID] *[a] and A. Bernardus Mostert [ID] *[b]

Eumelanin is a black-brown natural pigment found throughout nature. As a *material* class, it possesses unique physical and chemical properties that entice much attention from chemists, physicists, and material scientists due to its potential use in medical and sustainable organic (bio)electronics settings. To harness its potential, accurate spectroscopical characterization is a primary requirement for the efficient engineering of eumelanin-based electronic devices. A key spectroscopic technique is electron paramagnetic resonance (EPR) since the persistent paramagnetism of eumelanin is a spin-label signature of its molecular state. This review provides a comprehensive discussion on the origin of eumelanin paramagnetism through a multifrequency EPR approach and highlights the current multi-species point-of-view.

1. Introduction

Nature has employed organic matter as the base to develop complex systems capable of performing sensing, energy storage, light-harvesting, photoconversion, and free-radical scavenging. Inspired by these functional materials and their properties,

[a] São Paulo State University (UNESP), School of Sciences, Department of Physics and Meteorology, Bauru/SP, Brazil. E-mail: jv.paulin@unesp.br, carlos.graeff@unesp.br

[b] Department of Physics and Centre for Integrative Semiconductor Materials, Swansea University Bay Campus, Fabian Way, Swansea, SA1 8EN, UK. E-mail: a.b.mostert@swansea.ac.uk

humankind has been able to build all kinds of (bio)devices ranging from sensors, solar cells, ion-to-electron transducers, memory, and energy storage.[1–7]

Among a wide variety of candidates, melanins are one of the most thought-provoking bio-sourced materials in nature. It is a class of biological pigments of diverse chemical structures originating in animals from the oxidation and polymerization of tyrosine or in lower organisms from phenolic compounds.[5,8–10] In humans, the melanin class is split into black-brown eumelanin, reddish-yellow pheomelanin, and neuromelanin (spherical aggregates consisting of eumelanin encasing a central core of pheomelanin). These subclasses are variously responsible for

Dr João V. Paulin is a post-doctoral researcher at São Paulo State University (UNESP) in the Department of Physics and Meteorology. He earned his PhD in Science and Technology of Materials from UNESP, and his scientific contributions were recognized with the prestigious Thesis Award from the Coordination for the Improvement of Higher Education Personnel (CAPES). This award recognized his doctoral thesis as the best within the Materials field in Brazil

João V. Paulin

in 2021. Dr Paulin's expertise extends to the domains of Applied Physics. Currently, his research interests are at the intersection of biomaterials, sustainability, and organic (bio)electronics.

Carlos F.O. Graeff, PhD in Physics from UNICAMP (1994), is a Full Professor at UNESP since 2006. As a 1A CNPq fellow, Royal Society of Chemistry Fellow, and ACIESP member, he's globally recognized. With a rich career, he held positions like Vice President for Research at UNESP (2017-2021) and Higher Education Coordinator for São Paulo's State Government (2023). His expertise lies in Materials Science, focusing on electronic devices, biomaterials,

Carlos F. O. Graeff

and electronic magnetic resonance. Having supervised 50+ students and authored 200+ research articles, his impactful contributions extend to international collaborations and patents, reflecting a notable Scopus (ID: 57773923100) h-index of 34.
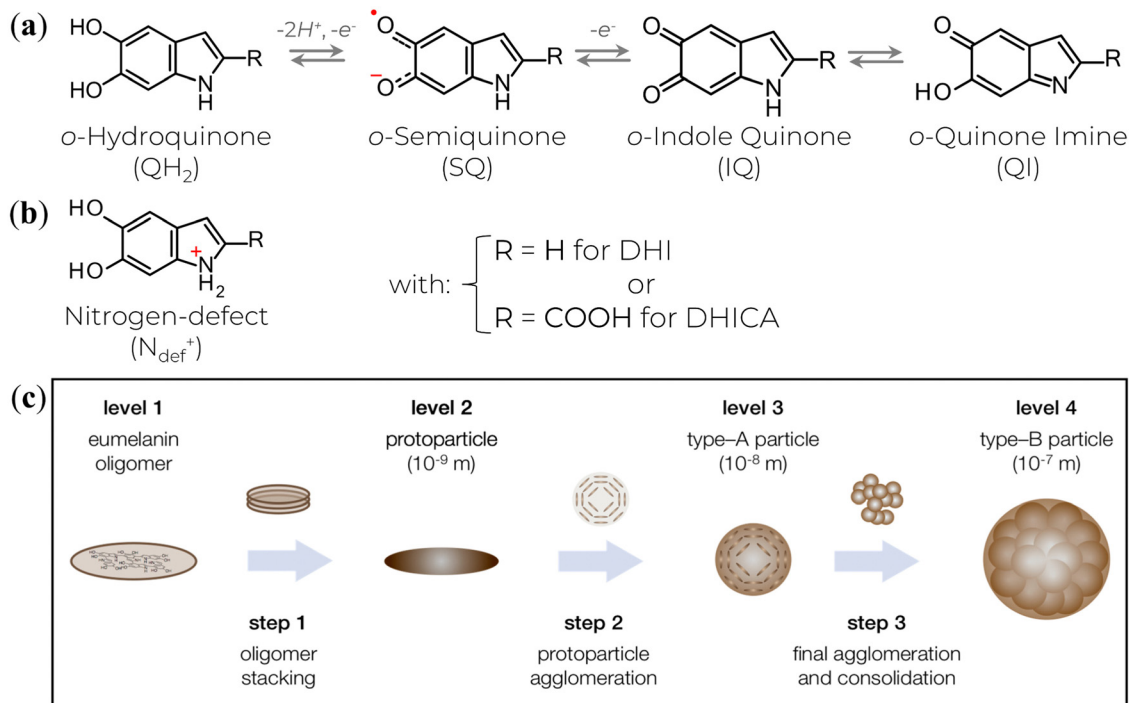
Fig. 1 (a) The various redox states and tautomers of eumelanin monomer building blocks. (b) A charged structure formed during the synthesis and aggregation steps. (c) The current three-step version for eumelanin particle formation. (c) is a reprint from A. Büngeler et al.[49] under Creative Common CC BY license.

antioxidant and anti-inflammatory functions as well as protection from harmful UV-light.[8,9,11] In addition, they are also of high medical relevance due to the potential relation to diseased states, such as melanoma (a type of skin cancer formed in the epidermal melanocytes),[12–14] Parkinson's disease[15–19] and Alzheimer's disease.[19,20]

Bernard Mostert is a materials scientist working on conductive biomaterials and bioelectronic devices. He received his PhD in Physics at the University of Queensland. He has held postdoctoral research positions at Lancaster University, University of Queensland and Swansea University. He has also been a recipient of the prestigious Marie Skłodowska-Curie fellowship. His specialty is understanding the charge transport mechanisms of biomaterials and devices as they are affected by the environment. He has over a decade of experience in pioneering hydration control experiments in diverse areas including both material and device electrical characterization, neutron and muon scattering and magnetic resonance measurements.

A. Bernardus Mostert

Melanins, especially the main subclass eumelanin, are also receiving attention in chemistry, physics, and materials science due to potential technological applications in biomedicine, organic electronics, and bioelectronics.[5,6,9] Indeed, several devices' platforms, such as electrochemical transistors,[21–23] energy storage,[24–27] memory,[28] optoelectronic skins,[29] phototransistors,[30] and sensors,[31–35] can be found in the literature. The variety of applications is attributable to the ability to form smooth and homogenous thin films[35–37] and to many relevant physicochemical properties, including UV-Vis broadband optical absorption, photoluminescence quantum efficiency to almost null, metal-ion chelation, radical scavenging, redox activity, paramagnetism, and hydration-dependent charge-transport.[5,6,8,9,11,38–40]

The physicochemical functionalities result from the highly heterogeneous nature of eumelanin's molecular and supramolecular structural features at the nano- and microscale. At the molecular level, the eumelanin class is assembled by chemically heterogeneous oligomers made up of 5,6-dihydroxyindole (DHI) and 5,6-dihydroxyindole-2-carboxylic acid (DHICA).[5,6,9,10] These monomer building blocks can undergo two processes of one-electron one-proton removal to be reversibly oxidized into their *ortho*-quinone forms and tautomers, Fig. 1a.[10,41,42] Synthetic intermediate residues such as uncyclized and charged structures (like the protonated nitrogen,[5,43] Fig. 1b) can also be found in eumelanin structure. These structures bind together, forming graphene-like layers of up to tens of units (Fig. 1c, Levels 1 & 2). Such layers are then self-assembled into nanoaggregates with different extensions *via* apparent π–π stacking and H-bonding in a combination of planar and twisted

segments (Fig. 1c, Level 3).[38] The characteristic stacking distances of $\sim$3.2–4.0 Å depend on hydration level and type of eumelanin.[44–48] Finally, the small aggregates agglomerate *via* edge-to-edge stacking (Fig. 1c, Level 4).

The high structural disorder and the low solubility hindered the design and engineering of eumelanin-based materials in earlier days due to challenges in precise characterization with traditional molecular chemical and physical methodologies. However, modern approaches indicate that UV-Vis, X-ray photoelectron spectroscopy (XPS), and electron paramagnetic resonance (EPR) techniques are the best primary tools for eumelanin's core characterization.[6]

Of particular interest to the present work, the EPR spectroscopic approach relies on eumelanin's strong and persistent electronic paramagnetic signal to obtain evidence of its structural and dynamic processes. Indeed, since the first report of eumelanin' EPR signal in 1954,[50] numerous papers have covered a wide range of paramagnetic responses to physical parameter changes. However, the precise nature of the paramagnetic signal in eumelanin still needs to be clarified. This review aims to provide a comprehensive understanding of the eumelanin paramagnetic system using multi-frequency EPR in both solution and solid-state. The in-depth analysis presented herein will illuminate the current state-of-the-art knowledge of eumelanin's paramagnetic signal, including its origins and potential future research directions.

2. Overview of EPR spectroscopy

EPR is a spectroscopy technique used to probe systems with paramagnetic centers (*i.e.*, unpaired spin states) such as free-radicals, ionic radicals, and molecules in triplet states. It can explore the chemical structure of these species, their interactions with the chemical environment, and the dynamics of processes in which they may be involved.[51–55]

This technique is based on the absorption of electromagnetic radiation, usually in the microwave frequency region, by a paramagnetic sample in the presence of an external magnetic field. The presence of the external magnetic field is commonly a necessary condition for the occurrence of the Zeeman effect, which is the splitting of paramagnetic levels for the different spin states of a sample; in other words, the magnetic field breaks the degeneracy of the spin states. Nonetheless, zero-field EPR signals are observed in specific cases.[56]

As a quantum mechanical construction, EPR spectroscopy uses the spin Hamiltonian to describe all the magnetic interactions of the spin with its surrounding environment. For a paramagnetic species at the ground energetic state with an electron spin S and n nuclei of spin I, the static spin Hamiltonian ($\mathscr{H}_0$) will be a contribution of the electronic spin with the external magnetic fields and internal magnetic moments[57] given by,

$$\mathscr{H}_0 = \mathscr{H}_{EZ} + \mathscr{H}_{HF} + \mathscr{H}_{NZ} \tag{1}$$

The different terms in eqn (1) indicate the electron Zeeman interaction ($\mathscr{H}_{EZ}$), electronic and nuclear spins hyperfine couplings ($\mathscr{H}_{HF}$), nuclear Zeeman interactions ($\mathscr{H}_{NZ}$). For the

following term descriptions, we will show conventional forms utilizing the Cartesian spin vector operator $\boldsymbol{S}^T = (S_x, S_y, S_z)^T$, with T indicating the matrix transpose.

The electron Zeeman term (eqn (2)), which represents the interaction between the electron spin and the external magnetic field $\boldsymbol{B}$,[52–55,58] is the dominant term of $\mathscr{H}_0$.

$$\mathscr{H}_{EZ} = \frac{\beta_e}{\hbar}\boldsymbol{B}^T\boldsymbol{g}\boldsymbol{S} \tag{2}$$

In eqn (2), $\beta_e\left(=\dfrac{e\hbar}{2m_e}\right)$ is an atomic unit of the magnetic moment called the Bohr magneton. The parameters e, $\hbar$ and m_e represent the values of the electron fundamental charge, the reduced Planck's constant (*i.e.*, $h/2\pi$) and the electron mass respectively. $\boldsymbol{S}$ represents the spin angular momentum. Since $\boldsymbol{S}$ and $\boldsymbol{B}$ are orientation-dependent, the magnetic dipole moment $\boldsymbol{g}$ (denoted by g-factor or g-value) will assume the general form of a tensor that in the radical molecular coordinate system results in eqn (3) or (4) if the orientation-dependence is averaged by fast molecular motion (*i.e.*, isotropic g-value).[53,55]

$$\boldsymbol{g} = \begin{pmatrix} g_{xx} & 0 & 0 \\ 0 & g_{yy} & 0 \\ 0 & 0 & g_{zz} \end{pmatrix} \tag{3}$$

$$g_{iso} = \frac{1}{3}(g_{xx} + g_{yy} + g_{zz}) \tag{4}$$

The interaction between the magnetic dipole of unpaired electrons and the nuclear spin in its vicinity is characterized by the hyperfine interaction $\mathscr{H}_{HF}$ (eqn (5)).[52–55,59] This interaction brings direct information about the magnetic environment of the spin.

$$\mathscr{H}_{HF} = \sum_k \boldsymbol{A}_k \boldsymbol{S}_k^T \cdot \boldsymbol{I}_k \tag{5}$$

where $\boldsymbol{I}$ is the spin quantum number of the kth coupled nucleus, and $\boldsymbol{A}$ is the hyperfine coupling interaction. $\boldsymbol{A}$ can be split into two main contributions: isotropic and anisotropic parts. The isotropic hyperfine (a_{iso}) is a through-bond interaction, described by eqn (6), that permits the outline of the spin delocalization onto molecular structure.[52,53,55]

$$a_{iso} = \frac{2\mu_0}{3\hbar}g_e\beta_e g_n\beta_n|\psi(0)|^2 \tag{6}$$

with the g_n being the nuclear g-value, β_n the nuclear magneton, μ_0 vacuum permeability. g_e is the g-value of a free electron, a fundamental constant accurately equivalent to 2.0023193043617(15).[60] The square of the wavefunction ($|\psi(0)|^2$) represents the electron wavefunction at the nucleus point, *i.e.*, spin density at the nucleus. Only radicals with an s-orbital symmetry will give a non-zero wavefunction contribution, hence the label of isotropic. On the other hand, the anisotropic part is a pure oriented magnetic dipole–dipole interaction detected only in solid-state and it is often used to obtain spatial information.[52,53,55,59]

Like the electron Zeeman splitting, the nuclear Zeeman term (eqn (7)) describes the coupling of the nucleus spin with the

external magnetic field.[53,55,59] However, it can be a few orders of magnitude lower than the $\mathscr{H}_{EZ}$ due to the smaller gyromagnetic ratio.[59]

$$\mathcal{H}_{NZ} = -\frac{\beta_e}{\hbar} \sum_k g_{n,k} \boldsymbol{B}^T \boldsymbol{I}_k \qquad (7)$$

Experimentally, a static magnetic field is varied across the sample to align the electronic spin in a specific direction, while a perpendicular microwave frequency is kept fixed. Hence, the microwave's absorption will only occur when the energy $h\nu$ of the radiation coincides with the energy difference (ΔE) between the spin states,[51–53] causing the spin to flip in the opposite direction of the polarizing field. The resonance condition (eqn (8)) determines the energy needed for this spin flip.

$$h\nu = \Delta E = E_\alpha - E_\gamma = g_e \beta_e B_0 \qquad (8)$$

with h corresponding to the Planck constant, ν to the resonance frequency, and E_α and E_γ to the spin energies levels, $E_\alpha > E_\gamma$, Fig. 2a.

As mentioned above, due to the spin–orbit coupling of the electron residing on a molecule, its g-value will deviate from the g_e and can display an anisotropic character; that is, the system will undergo different interactions of the magnetic field depending on the molecule's orientation axis. As a result, different g-values for each molecular axis will be obtained, i.e., $g_{xx} \neq g_{yy} \neq g_{zz}$ (rhombic symmetry). However, in many organic materials, paramagnetic systems have little spin–orbit interaction, and the value of the effective g-value is independent of the magnetic field direction. When the effective g-value is identical across all sample axes, $g_{xx} = g_{yy} = g_{zz} = g_i$, it is said to have isotropic symmetry.[51–53,55] An intermediary condition is also possible. In this case, the symmetry is uniaxial, with

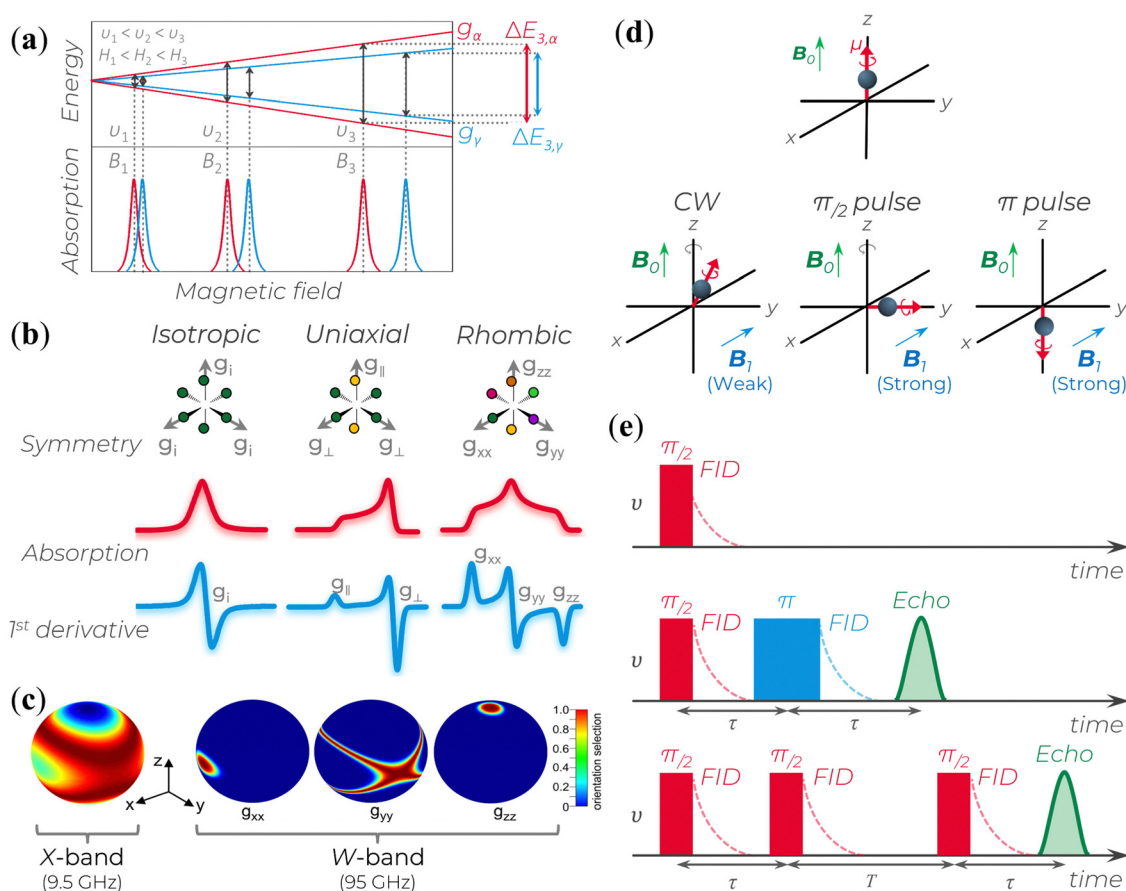Fig. 2 (a) Splitting of the energy levels of a two-spin system with isotropic lineshapes and similar g-values. At ν_i, the microwave frequency (or the corresponding B_i magnetic field), the two EPR lines almost completely overlap; as ν_i (or B_i) increases, the two lines get more separated. g_α and g_γ represents the g-values of two different spins. The splitting behavior represents the enhanced spectral resolution of high-frequency/high-field EPR (HFEPR). (b) Schematic relation of a powder paramagnetic system based on different symmetry condition and their respective absorption and first derivative EPR spectra for $S = \frac{1}{2}$. (c) Enhanced orientational selectivity of disordered materials by HFEPR. It is possible to determine the orientations of the dominant interaction tensor in spin systems that are randomly oriented and have a small g-anisotropy as long as the anisotropy of the primary interaction in the spin Hamiltonian exceeds the inhomogeneous linewidth. Reprinted with permission from K. Möbius et al. (2013).[58] Copyright© 2013, Elsevier. (d) B_0 indicates the direction of the polarizing field along which a magnetic dipole moment becomes aligned. The B_1 field induces magnetic interactions. B_1 applies a torque to the electron's magnetic dipole, resulting in a deviation from the B_0 axis. This deviation can be small (in CW experiments) or large (in pulse experiments). If the magnetic moment is aligned with or opposite to the B_0 field (as in π pulse case), there is no gyroscopic precession around the z-axis due to the electron spin. (e) Three common signal types generated in pulse EPR experiments: (top) free-induction decay (FID), (middle) echoes generated using a two-pulse sequence, and (bottom) echoes generated using a three-pulse sequence.

$g_{xx} = g_{yy} \neq g_{zz}$ or $g_{xx} \neq g_{yy} = g_{zz}$. Here, the unique g-value is ascribed as "$g_{\parallel}$" (g parallel), whereas the other two are "$g_{\perp}$" (g perpendicular). The overall absorption shape will be altered depending on the symmetrical orientations (Fig. 2b).

The microwaves' absorption is obtained by varying the magnetic field during data collection. Empirically, this absorption results in a Gaussian-like line shape shown in Fig. 2b. However, since the measurement is carried out with a modulated oscillating magnetic field and lock-in detection, the signal obtained corresponds to the first derivative of the absorption (Fig. 2b).[51–53] Based on this representation, the main experimental parameters are the signal lineshape, the number of peaks, the resonant magnetic field B_0 position, the linewidth, and the peak-to-peak signal amplitude.

At low microwave power (P), the EPR signal intensity (Y) can increase proportionally to $\sqrt{P}$ due to the absence of perturbation on the equilibrium of the spin state population. However, as P continues to increase, the signal eventually reaches a saturation point, after which it may either continue to increase or start to decrease.[51,52,61–63] This behavior is described by eqn (9).

$$Y = \sum_i \frac{C_i\sqrt{P}}{\left(1 + \dfrac{P}{P_{\frac{1}{2}^{,i}}}\right)^{\frac{b_i}{2}}} \tag{9}$$

$$P_{\frac{1}{2}} = \left(K\gamma^2 T_1 T_2\right)^{-1} \tag{10}$$

where C_i is a constant proportional to the spin density, $P_{\frac{1}{2}}$ is the microwave power at which the saturation effect reduces the signal intensity by half, and b_i represents the inhomogeneity parameter and can assume values from 1 (inhomogeneously broadened line) to 3 (homogeneously broadened line).[51,52,61–63] eqn (10) indicates that $P_{\frac{1}{2}}$ depends on a constant K related to the resonator's quality (Q)-factor, the gyromagnetic ratio γ for an electron, and the relaxation rates T_1 and T_2.[62] T_1, known as spin–lattice (or longitudinal) relaxation time, refers to the rate at which excited spin states relax back to the low-energy state due to interaction with the surroundings.[51,52,63] On the other hand, T_2, also called spin–spin (or transverse) relaxation time, arises from the interaction between the excited electron and other electrons or magnetic nuclei, which results in the dephasing of coherent electron spins without energy dissipation to the lattice.[51,52,63] We note that conventially the spin–spin relaxation rate has two separate representations, T_2 and T_2^*. The former is considered the true value for spin–spin relaxation times, whereas the latter is considered a value that is convoluted with some spin–lattice relaxation component. T_2 is usually only obtainable via pulsed EPR (see below). As such, technically, the spin–spin relaxation value in eqn (10) is a T_2^* value.

In addition to the experimental parameters and spectral behavior, another helpful parameter is the spin concentration in a sample. For the spin concentration determination, the signal from the studied sample is compared to a standard model containing a known spin number to minimize errors.[64] In this way, the spin concentration (ρ_N) can be estimated using eqn (11), where it considers the area A_{RC} under the resonance curve, a constant C_E specific to each spectrometer, the temperature T, the modulation amplitude A_M, and the applied microwave power P.[52,64]

$$\rho_N = A_{RC}\frac{C_E T}{A_M\sqrt{P}} \tag{11}$$

As eqn (11) is based on the double integral of the EPR spectra first-derivative, it is expected to obtain good baselines on both sides of the spectrum (i.e., low and high-field sides). Indeed, a constant baseline is required or, at least, a baseline correction after each integration.[52,64] Additionally, extended measurements far from the signal center should be used to minimize potential error resulting from finite truncation, especially for the extensive wings of Lorentzian-shaped lines.[52]

The standard X-band EPR spectrum has limited resolution for disordered materials, and the broad lines may hide information on molecular orientation and magnetic parameters.[58] Hence, higher microwave frequencies and higher magnetic fields (above W-band) are often employed, Table 1.

High-frequency/high-field EPR (HFEPR) has two important characteristics:

(i) *Enhanced spectral (or g-value) resolution*: g-values are directly proportional to the EPR spectrometer microwave frequency. Hence, a higher external Zeeman field will be able to increase the resolution of the g-values in relation to the hyperfine coupling (Fig. 2a and Table 1) since it can separate the field-dependent spin interactions from the field-independent ones.

(ii) *Enhanced orientational selectivity in disordered samples*: materials with different spin–orbit coupling can yield different responses with respect to the Zeeman-field. Hence, as the external magnetic field is increased, a specific orientation relative to the high field is obtained, which enables

Table 1 Frequencies and resonance field for two different paramagnetic species with close g-values for different microwave bands available in EPR spectrometers

Microwave band	υ (GHz)	B_0 (mT) $g_{CCR} = 2.0032$	B_0 (mT) $g_{SFR} = 2.0045$
L	1	35.670	35.644
S	4	142.667	142.575
X	9	321.001	320.793
K	24	856.003	855.448
Q	35	1248.338	1247.528
U	50	1783.340	1782.183
V	65	2318.342	2316.838
E	75	2675.010	2673.275
W	95	3388.346	3386.148
F	111	3959.015	3956.447
D	140	4993.352	4990.113
—	190	6776.692	6772.297
—	265	9451.702	9445.572
J	285	10 165.038	10 158.445
—	360	12 840.048	12 831.720

differentiation of the *g*-tensor anisotropy (Fig. 2c), *i.e.*, the orientation of their main axes within the *g*-matrix system.

Additional advantages of HFEPR over standard EPR measurements are the enhancement in detection sensitivity for restricted-volume materials, enhancement for probing fast motion dynamics, and enhancement of low-temperature electron-spin polarization. For a detailed explanation of these particularities, the authors suggest to the readers the references.[55,58,59,65]

One efficient manner to obtain an EPR signal is through continuous wave (CW) methods, in which microwave or radio frequency (rf) fields are continuously applied. However, a drawback to this approach is that the resulting spectra have complete $\mathcal{H}_0$ information and often manifest overlapping contributions that are not easily resolved into individual components.[66,67] Therefore, pulse EPR is a powerful tool to precisely manipulate the spin system by applying microwave pulses of a specific frequency to induce transitions that contain only the desired $\mathcal{H}_0$ contribution of one particular spin system.[66,67]

During pulse EPR experiments, the spin evolution of the electron is recorded after applying a strong B_1 field for brief durations, typically ranging from tens to hundreds of nanoseconds, while maintaining a constant external magnetic field B_0. Compared to CW EPR, the B_1 pulses used are considerably more intense, allowing for a more pronounced tilting of the electron's magnetic moment into the *xy* plane in a short period of time (Fig. 2d). This tilting enables the precession and dephasing of electron spins around the *z*-axis within the same plane. To obtain the description of the spin evolution under the influence of applied pulses using quantum mechanics, visit the fundamental works.[51,66,67] Differences in the structural features of molecules that contain the unpaired spin or variations in the spin states of nearby magnetic nuclei can perturbate the precession frequency of each spin, leading to changes in the *g* and hyperfine coupling values.

In pulse EPR, there are several variations to generate and detect signals. The signal can be detected when the spin magnetic moments precess in the *xy* plane and add up to a total non-zero magnetic moment. A free induction decay (FID) signal can be observed after a π/2 pulse is applied along the *x*-axis. In this situation, the magnetic moment will gradually diminish in the *y* direction due to the different rates of the electron spin precession. This decrease is the FID (Fig. 2e, top). However, as a single microwave pulse is often insufficient to excite the broad spectra of a short-lived FID, a second pulse followed by a time τ twice as long as the first (Fig. 2e, middle) is applied to rephase the spins. This results in an echo signal that can be detected and analyzed. A stimulated echo can also be obtained using a third pulse at any time *T* after the second one (Fig. 2e, bottom). In a typical pulse EPR, the integrated FID or integrated echo intensity is collected as a function of another experimental variable (usually the magnetic field B_0).

The relaxation behavior (T_1 and T_2) are fundamental limitations in pulse EPR experiments, as T_1 dictates the speed at which an experiment can be repeated, and T_2 affects the persistence of the spin-echo, restricting the resolution of frequencies and the distances that the technique can measure.

For a detailed interpretation of the EPR signals, simulations can be used to accurately determine critical spectral features such as the *g* and hyperfine values. Among the various computational tools available, EasySpin is commonly used and is available as free software.[68,69] This computational package has several high-level functions that separate the resonance lines (*g*-value, linewidth, and intensity) of the paramagnetic species present in the studied systems and thus identify their spectroscopic characteristics. Not only that, but it is also possible to simulate EPR spectra with isotropic and/or anisotropic *g*-values, different line forms and linewidths, hyperfine interactions, and an arbitrary number of electronic and nuclear spins of samples in several physical states (powders, crystals or liquids) and experimental conditions (continuous or pulsed wave, low or high temperature).[68] WinSim,[70] XSophe,[71] and SpinDynamica[72] are other available options. In-house written simulation programs are also a possibility.

3. X-band EPR signal overview of eumelanin

The X-band EPR signal of eumelanin is usually reported by a slight asymmetric spectrum with a width of about 4–6 G, *g*-value ranging from 2.003–2.006, and no observable hyperfine coupling (Fig. 3a). Additionally, such spectra features are intriguing by being unusually broad for an organic radical and by being remarkably similar in different experimental conditions (hydrated
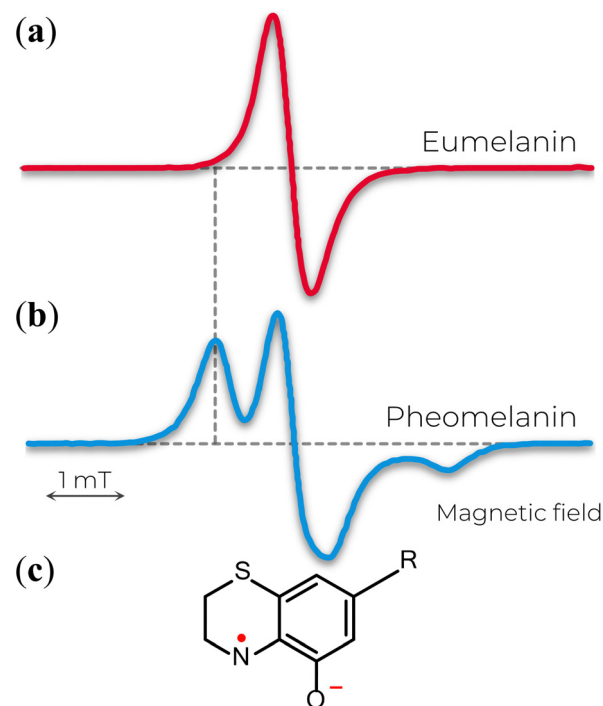

Fig. 3 X-band EPR spectra of (a) eumelanin and (b) pheomelanin. The extra feature in *b* is attributed to the nitrogen hyperfine coupling of (c) *o*-semiquinonimine. (a) Adapted with permission from J.V. Paulin *et al.* (2019).[78] Copyright© 2019, American Chemical Society. (b) Adapted with permission from A. Zadlo *et al.* (2018).[79] Copyright© 2018, John Wiley & Sons.

suspensions or solid-state) and sample source (natural or synthetic). This behavior made the EPR technique an efficient tool for identifying different melanins (eu- and pheomelanin) in pigmented systems (*e.g.*, eye, hair, and skin).[73,74] The difference that allows such differentiation arises from the 1,4-benzothiazine subunits in pheomelanin, which provides a distinct hyperfine coupling from a partial localization of the unpaired electron on the nitrogen atom of the *o*-semiquinonimine (Fig. 3b and c).[75] The featureless EPR signal of eumelanin is the result of inhomogeneous broadening of the lineshape that hinders the amount of information one can get, especially the hyperfine interactions from immobilized randomly oriented *o*-semiquinone radicals[76] and the various hyperfine couplings of the protons in the eumelanin subunits.[77]

The nature of the EPR signal of eumelanin has been speculated in the seminal paper of M.S. Blois and co-workers back in 1964.[80] They proposed three possibilities: transition element ions, semiconductor-like behavior, and triplet-singlet band overlap. The first case was quickly ruled out by the similarities between natural and ultra-pure synthetic eumelanin (Fig. 4, as examples),[80–82] which indicates that the unpaired electrons should arise from a common origin. The semiconductor model was rejected as the free-radical concentration in the dry state does not follow an exponential function with temperature, implying that the thermally excited electrons cannot be the origin of the eumelanin resonance.[80] In the same line, the observed *g*-values suggest that the unpaired electron would be restricted to one or two monomeric units.[83] In the case of the triplet–singlet band model, an extensive conjugation length would be a necessary condition; however, this is not the case. The EPR signal did not suffer any alteration when ascorbic acid was used to reduce the conjugation, and the spin–lattice relaxation values were large, which would be counter-intuitive if dealing with conjugation. Also, a higher concentration of cupric ions can quench the eumelanin's signal. Such a behavior would be an odd feature if they were just splitting the overlapping bands.[80] Later studies on temperature-dependent EPR measurements on eumelanin hydrated suspension agree that the spectroscopy features (*g*-value) do not fit with the triplet idea.[84] Instead, it suggests that the unpaired electron should be restricted to a few monomeric units in radical or biradical states.[80,84] The idea of the eumelanin's paramagnetism being part of monomeric units remains strong to the current date, and several models were built on it.

A key point of eumelanin's EPR signal is that it is extremely persistent; however, the free-radical concentration is not. Indeed, only the degradation of the eumelanin backbone structure was able to quench its EPR signal irreversibly.[80] As an example of changes in the EPR signal, we turn our attention to the pH effect of Dopa-Eumelanin shown in Fig. 4. As the pH increases from low (pH 1) to high (pH 12), the *g*-values range from 2.0034 to 2.0042, and the EPR signal becomes narrower and more asymmetric.[82] Additionally, it is possible to observe variation in the spin concentration (2.0×10^{18} at pH 2 to 1.2×10^{19} at pH 12).[82] Similar changes can be seen in Cu^{2+}-eumelanin complexes where the free radical's *g*-value and intensity show similar pH dependent behavior as for the uncomplexed material.[85] However, a key difference is that the line shape

Fig. 4 Effect of pH on (a) *g*-value, (b) linewidth, and (c) spin concentration of natural Bovine eye pigment (majoritarian eumelanin) and synthetic Dopa-Eumelanin. (a)–(c) Adapted with permission from S-S Chio *et al.* (1982).[82] Copyright© 1982, Elsevier Inc.

broadens due to the presence of the Cu^{2+}.[85] This allows investigation of how the radical centers bind to metal cores (see below). Other external agents can also change the eumelanin EPR signal, as presented in Table 2. In Table 3, we provide a

Table 2 Alteration on the EPR signal of eumelanin and eumelanin-based materials by different physicochemical agents

Eumelanin	Experimental condition	Physicochemical agent	Spectral alteration	Ref.
Bovine eye Eumelanin	- CW[a] - 9.5 GHz - FM: 100 kHz - 296 K - Suspension	- Visible light (not specified)	- Reversible photo induced radical observed. - Photo induced radical stabilized in alkaline solution.	86
Bovine-eye (Primarily eumelanin) Dopa-Eumelanin	- CW[a] - 9.5 GHz - FM: 100 kHz - Dark/light - Aqueous suspensions - ~ pH 7	- Visible light (not specified) - pH (pH 1 to pH 10.5, both light and dark) - Dissolved aqueous O_2 (0–100 %)	- Reversible ΔY_{PP} increase with light. - Increase in signal after a plateau in pH curve. - Additional increase in signal with light. - Reversible increase in signal with increasing O_2. - No change in signal for dried bovine-eye sample.	87
Dopa-Eumelanin Human skin pigment Black human hair eumelanin	- CW[a] - 9.3 GHz - FM: 100 kHz - Suspensions (Dopa) - Solid State (Skin and Hair) - 100 K (Dopa) - 77 K (Skin and Hair)	- Light (Dopa: Visible Light at 200 W cm^{-2}; Human skin pigment: 600–700 nm at 200 W cm^{-2}; Black hair: Visible Light at 300 W cm^{-2}) - Microwave Power - Hydration (Black human hair: Dry and wet)	- MWP data shows an increase, saturation and then a decrease in signal intensity. - Power saturation curves are offset by a constant (on a log scale) to a higher signal intensity after irradiation of all samples. - Wet hair showed a bigger signal increase after irradiation vis-à-vis dry sample. - Wet sample had lower signal intensity than dry sample before irradiation.	88
Squid-ink (*Logigo opalescens*) in Calcium-Magnesium salt form ("*A*-melanin") Squid-ink (*Logigo opalescens*) Calcium & Magnesium removed ("*B*-melanin") Harding-Passey mouse melanome Human hair-eumelanin (alkaline extraction) Human hair-eumelanin (intact hair) Potato-eumelanin *o*-hydroquinone (catechol)-Eumelanin (auto-oxidation and enzyme oxidized) *p*-hydroquinone-eumelanin (auto-oxidation and enzyme oxidized) *m*-hydroquinone (resorcinol)-eumelanin (auto-oxidation and enzyme oxidized) L-Dopa-Eumelanin (auto-oxidation and enzyme oxidized) D-Dopa-Eumelanin (auto-oxidation and enzyme oxidized) L-adrenalin-eumelanin (auto-oxidation and enzyme oxidized)	- CW[a] - 9–10 GHz - FM: 100 kHz - MWP: 4–100 mW (most experiments) - MWP: 10–1000 μW (B-melanin, at 77 & 295 K) - Powders	- Metal ion (Cu^{2+}) - Temperature (4.2 K, 77 K, 295 K, 450 K, 500 K) - Hydration (Dry & Wet [0–30% by weight]) - UV irradiated (55 min, unfiltered)	- Generally, auto-oxidized and enzyme-oxidized materials spectra taken at 295 K fell within a g_{iso} of ~2.0036–2.0040. - Generally, eumelanins from natural sources have a broader range of g_{iso} values of 2.0030–2.0048. - A-melanin lineshape in-between Gaussian and Lorentzian shapes, with a slight asymmetry. - A-melanin g_{iso} is pretty insensitive to temperature. Line width increases with lowering temperature. - A-melanin g_{iso} slight increase with Cu addition, with a significant increase in line width. - Ink from *Logigo opalescens* has a lower spin concentration than *Sepia officinalis*. - B-melanin and Cu-doped A-melanin exhibit Curie–Weiss law temperature dependence. - B-melanin line width broadens with decreasing temperature. - T_2 relaxation times are similar between all samples and MWP insensitive (CW-EPR inferred). - T_1 relaxation times for A & B melanins varied depending on MWP. - T_1 relaxation times for A-melanin decreased with increasing copper content. - T_1 relaxation times for B-melanin increased with decreasing temperature. - There is an effect on T_1 relaxation times due to hydration. - Decrease in signal amplitude with increased Cu^{2+} concentration for A-melanin and hydroquinone. Most detail on A-melanin. - Decrease in signal for Cu-doped A-melanin when hydrated.	80
Bovine-eye (With protein (*A*-type) and without protein (*B*-type))	- CW[a] - 9–10 GHz - Aqueous suspensions - 295 K	- Metal ions (Mn^{2+}, Cu^{2+}, Ni^{2+}, Co^{2+}, Gd^{3+}, Ho^{3+}, Tm^{3+}, Dy^{3+}, Er^{3+}, Nd^{3+}, Sm^{3+}, Pr^{3+})	- Decrease in signal amplitude with increasing concentration. - Increase in $P_{\frac{1}{2}}$ with increasing concentration. - Effects are more muted in B-type *vs.* A-type. - Binding of Gd^{3+} preferential to eumelanin *vs.* ethylenediaminetetraacetic acid.	89

Table 2 (continued)

Eumelanin	Experimental condition	Physicochemical agent	Spectral alteration	Ref.
Bovine-eye Dopa-Eumelanin	- CW^a - 9.5 GHz - FM: 100 kHz - MWP: 20 μW to 200 mW - Aqueous suspensions - pH 5.5 - 77 K and room temperature	- Metal ions (Mg^{2+}, Ca^{2+}, Sr^{2+}, Zn^{2+}, Cd^{2+}, Al^{3+}, Sc^{3+}, La^{3+}, In^{3+})	- Increase in signal amplitude. - Higher g-value for Bovine *vs.* dopa samples. - Reversible complexation of metal ions with the eumelanin. - Generally, no to small lower changes in g-values relative to Bovine melanin upon complexation - Generally higher g-values for synthetic samples upon complexation. - Predominantly an increase in linewidth upon complexation. - Generally, a decrease in $P_{\frac{1}{2}}$ for bovine eumelanin upon chelation. - Similar $P_{\frac{1}{2}}$ values were observed for Dopa-Eumelanin upon chelation. - Smallest increases in signal are for alkaline earth metal ions.	90
Dopa-Eumelanin	- CW^a - 9–10 GHz^a - MWP: Power saturation experiment - 298 K - Suspensions	- Microwave Power - O_2 (Oxygenated, aerated & deoxygenated) - UV-Visible Light (Filtered light of - 320-600 nm) - Spin Traps (Superoxide dismutase, catalase, DMPO)	- MWP saturation point with associated high power signal attenuation increases with oxygen content in solution. - Line shape independent of oxygen content. - With irradiation, oxygenated samples' power saturation point decreases.	91
Bovine eye eumelanin (with protein) Bovine eye eumelanin (reduced protein content)	- CW^a - 9–10 GHz^a - FM: 100 kHz - Solid state (powder) - Suspensions - Power saturation recovery experiments	- pH (acidic (0.5 M in HCl) and basic - (0.5 M in KOH)) - Metal ion content (0.5 M Zn^{2+}) - Temperature (123 K, 193 K, 303 K)	- $\Delta H_{\frac{1}{2}}$ and spin lattice relaxation time increase with decreasing temperature. - $P_{\frac{1}{2}}$ decreases with decreases with temperature. - Free radical concentration did not change with temperature. - $\Delta H_{\frac{1}{2}}$ and $P_{\frac{1}{2}}$ decrease going from solid to suspension (any suspension). - pH had greater effect on $\Delta H_{\frac{1}{2}}$ than Zn^{2+}. - Spin concentration: alkaline > solid > Zn^{2+} > pH 6 > acidic. - $\Delta H_{\frac{1}{2}}$ increase going from material with protein to without protein. - Protein free had higher spin concentration.	92
Bovine-eye Dopa-Eumelanin	- CW^a - Time-resolved EPR - Dark/Light - Deoxygenated aqueous suspension - pH 7 - 77 K and 353 K	- UV-vis light (320-600 nm)	- Increase in g-values and lineshape. - Significant enhancement on microwave saturation characteristics.	93
Bovine-eye Dopa-Eumelanin	- CW^a - 9–10 GHz - FM: 100 kHz - Aqueous suspensions - pH 7	- Temperature (77–353 K)	- Spin concentration is temperature-dependent, with a decrease with increasing temperature. Arrhenius behavior in liquid solution. There is no change when the solution is frozen. - $\Delta H_{\frac{1}{2}}$ is temperature-independent for frozen suspensions. - $\Delta H_{\frac{1}{2}}$ decrease for $T > 273$ K.	84
Catechol-Eumelanin Dopa-Eumelanin	- CW^a - 9–10 GHz^a - FM: 100 kHz - MA 5 G - MWP: 5 mW - 77 K - Complexed to Cu^{2+} - Suspensions	- pH (pH 2 to pH 10.7)	- g-value increases from pH 2.0 to pH of 10.7. - ΔY_{PP} has slow decrease with pH and then under alkaline conditions (> pH 8) rapidly increases up to 5 times to initial acidic signal. - $\Delta H_{\frac{1}{2}}$ increases with pH under concentrated acidic conditions and then levels off. - Dopa-Eumelanin has an overall broader signal compared to Catechol-Eumelanin. - $P_{\frac{1}{2}}$ decreases with increasing pH, with a similar qualitative trend in size as $\Delta H_{\frac{1}{2}}$.	85
Dopa-Eumelanin (neat, oxidized, reduced and methylated) Bovine eye eumelanin (with protein and reduced protein content)	- CW^a - 9–10 GHz^a - FM: 100 kHz - MA: 1.6 G - MWP: 1 mW - 296 K - Suspensions	- pH (pH 5.5 to pH 12) - O_2 (Native consumption monitored) - Spin Traps - (3-carbamoyl-2,2,5,5-tetramethyl-3-pyrroline-1-yloxy) - Visible light (power 360 W m^{-2})	- Eumelanin consumes oxygen, especially SFR.	94
Bovine-eye Dopa-Eumelanin	- CW^a - 9.3 GHz - FM: 100 kHz - MWP: 50 μW - Aqueous suspensions	- pH (pH 1 to pH 12) - Temperature (278–353 K)	- Increase in free-radical concentration after a plateau. - g-value and concentration increase with pH. - $\Delta H_{\frac{1}{2}}$ decreases with pH. - Radical concentration higher in Dopa-Eumelanin *vs.* Bovine-eye Eumelanin.	82

Table 2 (continued)

Eumelanin	Experimental condition	Physicochemical agent	Spectral alteration	Ref.
	- 296 K (pH isotherm results) - 278–353 K - pH 1 to 12		- Apparent Arrhenius behavior. - Increasing Arrhenius constant with increasing pH. - Increasing enthalpy with pH up to neutral, then there is a slight decrease.	
Human hair-Eumelanin	- CW[a] - 9.52 GHz - FM: 100 kHz - MA: 0.5–2 G - MWP: 7.6 mW - KBr pellets - Initial 296 K - Poly or monochromatic - Aqueous solution	- UV-vis light - (280–560 nm) - Temperature - ($\sim$120–500 K) - pH (Low, neutral and high) - pH (pH 0 to pH 13)	- Increase in the signal intensity. - At low temperatures, the signal decreases with increasing temperature (Curie–Weiss law). - Signal increases at higher temperatures. - Low pH, decrease in signal intensity, line width remains same vis-à-vis neutral. - High pH, increase in signal intensity, line width increases. - In an aqueous solution, the signal increases, and there is no change in line width.	95
Bovine-eye Dopa-Eumelanin	- CW[a] - 9.5 GHz - FM: 100 kHz - MA: 8 G - MWP: 1 mW - 296 K - Dark/Light - Aqueous suspension - pH 7.6	- UV-vis light (230-600 nm)	- Increase in signal intensity. - Increasing O_2 content does not lead to an increase in radical production. - Radical formation is higher for natural eumelanin - Radical production is more effective at shorter wavelengths. - Proteins in natural eumelanin had no effect in generating light-induced radicals.	96
Bovine-eye Dopa-Eumelanin	- CW[a] - Aqueous suspension - pH 7.6	- UV-vis light (250 and 544 nm)	- Increase in free-radical concentration.	97
Dopa-Eumelanin (auto-oxidation and enzyme oxidation) Bovine-eye Eumelanin	- CW[a] - 9–10 GHz[a] - FM: 100 kHz - 298 K - Initial suspensions in PBS (pH 7.6)	- UV-Visible Light (230-580 nm) - Spin Traps (Nitroxides) - pH (pH 5 to pH 10)	- Rate of reaction increases with pH. - Oxidation and reduction of the eumelanins under light conditions depending on wavelength and spin trap compound.	98
Dopa-Eumelanin	- CW[a] - 35 GHz - Aqueous suspensions - 233 K	- pH (pH 3 to pH 12)	- Increase in linewidth and g-values. - Low anisotropy in acid and neutral pH. - Moderate anisotropy at higher pH. - Increase in total spin concentration with pH.	99
Dopa-Eumelanin (auto-oxidation and enzyme oxidation) Bovine-eye eumelanin	- CW[a] - 9.5 GHz - FM: 100 kHz - MWP: 1 mW (eumelanin radicals), and 20 mW (Phosphate buffer solution; 0.1 M, pH 8.0). - 296 K	- Superoxide anion (Potassium superoxide in dimethyl sulfoxide) pH (pH 7.5 to pH 9.7)	- Higher spin concentration for Dopa-Eumelanin vs. Bovine-eye eumelanin. - Increase in linewidth and g-values. - Increase in EPR signal amplitude. - Superoxide-induced eumelanin radical formation rate following: auto-oxidized eumelanin > enzyme-oxidized eumelanin > bovine eumelanin. - Rate of formation is linearly dependent on eumelanin and superoxide concentrations. - Rate of formation increased with pH. - Increase in radical concentration as a function of Mg^{2+} concentration. - The rate of induced radicals reduces in the presence of Mg^{2+}. - Similar effects seen in Ca^{2+} and Zn^{2+} as for Mg^{2+}.	100
Human red hair	CW[a] - 9.75 GHz -298 K[a] - Solid state	- Relative Humidity (Dry, 32.3%, 58% and 79.8%) - Visible light (UV and infrared filtered, 50 mW.cm^{-2})	- Radical concentration decreases with increasing humidity. - Light induced radical concentration increases with increasing humidity. - Decay of light induced radicals increases with increasing humidity.	101
Dopa-Eumelanin	- CW[a] - 9 GHz - FM: 100 kHz - MA: 3.3 G - MWP: 1 mW - Time constant: 0.25 s - Scan rate: 4 min	- 4-MeO-PhN$_2$BF$_4$	- Increase in relative (i.e., vs. 4-MeO-PhN$_2{}^+$) signal amplitude with increasing concentration for [4-MeO-PhN$_2{}^+$] < 2 mM. - [4-MeO-PhN$_2{}^+$] > 2 mM, relative EPR signal amplitude reaches a plateau.	102

Table 2 (*continued*)

Eumelanin	Experimental condition	Physicochemical agent	Spectral alteration	Ref.
	- Phosphate buffer solution (50 mM, pH 7.0) - 296 K			
Dopa-Eumelanin	- CW[a] - X-Band - FM: 100 kHz - MA: 0.5–3 G - MWP: 1 or 10 mW - Dark/Light - DMPO and benzophenone in water/ethanol (1:1), deaerated	- UV light (366 nm)	- Benzophenone absence: reversible increase of eumelanin free-radical. - Benzophenone presence: unstable but persistent formation of photoinduced radicals even after the light is turned off; increase in signal intensity. - Radicals can be destroyed with continuous illumination.	103
Dopa-Eumelanin	- CW[a] - 9.4 GHz - FM: 100 kHz - Suspension at pH 4.6 - 296 K[a]	- Visible Light (> 300 nm)	- Increase in signal intensity upon illumination.	104
Dopa-Eumelanin (Centrifuged from pH 7.6) Dopa-Eumelanin (Acid treated and washed)	- CW[a] - 9.3 GHz - FM: 100 kHz -MWP: Power saturation experiment - 298 K - Powder samples	- Microwave Power (Attenuation 20 to 0.5 dB)	- Slight decrease in g-value, $\Delta H_{\frac{1}{2}}$, radical concentration and spin lattice relaxation from neutral sample to acid treated sample. - Slight increase in spin–spin relaxation time. - No clear discernable difference in power saturation.	105
Dopa-Eumelanin	- CW[a] - 9.1 GHz - Powder	- Temperature (333–373 K)	- Increase in g-values and linewidth. - Increase in spin-concentration and tend towards saturation with time. - Decrease of bounded water mass.	106
DHI-Eumelanin	- CW[a] - 9–10 GHz[a] - Suspension - 10 K	- pH (5.59–11.02)	- ΔY_{PP} increases with pH. - g-value shifts to higher values with increasing pH. - Line asymmetry become more pronounced with increasing pH.	107
Dopa-Eumelanin Bovine-eye Eumelanin	- CW[a] - 9–10 GHz[a] - FM: 100 kHz - MA: 2.0 G - MWP: 20 μW - 283 K - Suspension	- Light with time (390 nm–520 nm, 0.4 and 0.24 W cm^{-2})	- Signal intensity decreased with time, *i.e.*, photo bleaching was achieved over 200 h.	108
Dopa-Eumelanin	- CW[a] - 9.3 GHz - FM: 100 kHz - MWP: 0.7 mW and power saturation experiment - Solid-State - 298 K	- Metal ion (Cu^{2+} and Zn^{2+} content varied)	- a systematic higher g-value when Cu^{2+} present, but no trend in concentration. - g-value does not significantly change with Zn^2 addition. - Increased $\Delta H_{\frac{1}{2}}$ with Cu^{2+} and Zn^{2+} addition - Systematic decrease in spin concentration with increasing Cu^{2+}. - Systematic increase in spin concentration with increasing Zn^{2+}. - Power saturation observed for neat material, and then a decrease of signal intensity with power. - Line width of neat material increased linearly with MWP$^{\frac{1}{2}}$. - Intensity increased linearly with MWP$^{\frac{1}{2}}$ for Cu^{2+} containing material.	109
Human-eye (eumelanin and low concentration of pheomelanin)	- CW[a] - Time-resolved EPR - 9–10 GHz - Dark/Light - Oxygenated & deoxygenated aqueous solution.	- UV light (355 nm)	- Increase in signal intensity. - Slight increase in linewidth. - Negative baseline after light illumination observed, which recovers to the original baseline with time.	110
Dopa-Eumelanin	- CW[a] - 9.5 GHz	- Temperature (180–470 K)	- Sample was tested as prepared, heat treated to 373 K, cooled, and then tested.	111

Table 2 (continued)

Eumelanin	Experimental condition	Physicochemical agent	Spectral alteration	Ref.
	- Powder - Wet and dried	- Heat Treatment/ Annealing (373 K)	- Increase in g-values and linewidth after treatment. - Decrease in EPR signal intensity for $T < 350$ K. - Increase in EPR signal intensity for $T > 350$ K. - For wet sample at low temperatures, temperature dependence obeys Curie–Weiss law, *i.e.*, signal decrease with increasing temperature (180–350 K) - Signal increases at higher temperatures (350-470 K), linear in T^{-1}. - The dry sample has a relatively higher signal than the wet; it obeys the Curie–Weiss law (470–240 K).	
Dopa-Eumelanin	- CW^a - 9.5 GHz - FM: 100 kHz - MA: 0.1 mT - MWP: 5 mW - 298 K - Solid-State	- No specific variable	- g-value = 2.004. - $\Delta H_{\frac{1}{2}}$ = 0.45 mT.	112
DHI-Eumelanin DHICA-Eumelanin	- CW^a - 9 GHz - FM: 100 kHz - MA: 2.0 G - MWP: 0.6 mW and power saturated experiment - 298 K - Solid-State	- DHI *vs.* DHICA starting material. - Desiccated *vs.* Lyophilized	- g-values remained the same for poly-DHI and poly-DHICA. - $\Delta H_{\frac{1}{2}}$ not affected by preparation state, but it is broader for poly-DHI compared to poly-DHICA. - Preparation state did not show discernable trend in spin concentration changes. - Systematic decrease in spin concentration from poly-DHI to poly-DHICA. - Poly-DHICA power saturates under lower microwave power and then decreases quickly. In contrast poly-DHI power saturates at high microwave power and then decreases slowly.	38
Dopa-Eumelanin (acidic, neutral and alkaline)	- CW - 9–10 GHz - FM: 100 kHz - MA: 0.036 mT - MWP: 0.2 µW to 2 mW - Solid-state - Vacuum - H_2O vapor pressure	- pH (Acidic, neutral and alkaline) - Hydration (0 to 80% RH)	- Acid and neutral signal inferred to be dominated by CCR. - Alkaline signal has an additional feature, inferred as an SFR. - Spin concentration is modulated by pH. - Decrease in signal intensity with hydration. - ΔY_{PP} decreases with the increase in hydration for acidic and neutral samples. - ΔY_{PP} is independent of hydration for alkaline samples. - Spin concentration is modulated by hydration.	113
Dopa-Eumelanin (acidic, neutral and alkaline)	- CW - 9–10 GHz - FM: 100 kHz - MA: 0.036 mT - MWP: 2 µW to 2 mW - Solid-state - D_2O vapor pressure - 296 K	- Hydration (0 to 80% RH) - pH (Acidic, Neutral & Alkaline)	- Decrease in EPR signal intensity with hydration. - ΔY_{PP} decreases with the increase of hydration for acidic and neutral samples. - ΔY_{PP} is independent of hydration for alkaline samples. - Spin concentration is modulated by hydration. - Line width narrows with hydration for high pH sample. Probable reduction in hyperfine interaction with deuterium addition.	114
Dopa-Eumelanin	- CW - 9–10 GHz - FM: 100 kHz - MA: 0.25, 0.36 or 9.8 G - MWP: 0.063, 2, 199.2 or 585 mW - Solid-state - Vacuum - 296 K	- pH (Neutral and alkaline) - Hydration (0 to 80% RH) - Optical Light (White LED spectrum)	- Neutral EPR signal dominated by CCR (lower g-value inferred). - Alkaline EPR signal has an additional feature at a high g-value, inferred as SFR. - Ammonia treatment and MWP increase the relative strength of SFR. - Sample probed at low MWP gave a negative photo response when dry. The photo signal becomes systematically positive with increasing hydration. It is inferred as CCR behavior. - Sample probed at high MWP gave positive photo response in dry and wet conditions. Inferred as SFR behavior.	115
Tyrosinase Natural Eumelanin Tyrosinase Synthesized Dopa-Eumelanin Tv laccase Synthesized Dopa-Eumelanin	- CW^a - 3.9 GHz - FM: 100 kHz - MA: 0.2 mT - MWP: 1.90 mW - 296 K - Solid state (powder)	- Multifrequency experiment	- At 3.9 GHz: Natural eumelanin has a higher g-value *vs.* synthetic material. - At 9.8 GHz: $\Delta H_{\frac{1}{2}}$ is larger for the natural eumelanin *vs.* synthetic material.	116
Tyrosinase Natural Eumelanin	- CW^a - 33.9 GHz	- Multifrequency experiment	- Complex spectra *vs.* S and X band data. Consistent with multiple species but not sufficient to resolve the species spectra.	116

Table 2 (continued)

Eumelanin	Experimental condition	Physicochemical agent	Spectral alteration	Ref.
Tyrosinase Synthesized Dopa Eumelanin Tv laccase Synthesized Dopa Eumelanin	- FM: 50 kHz - MA: 0.2 mT - MWP: 0.06 mW - 296 K - Solid state (powder)			
Dopa-Eumelanin Oxidized Dopa-Eumelanin	- CW - 9.3 GHz - FM: 100 kHz - MA: 0.025 mT - MWP: 0.03 and 10 mW - Solid-state (Pellets)	- Hydration (0 and 80% RH)	- Decrease in EPR signal intensity with hydration. - g-value statistically independent on hydration. - ΔY_{PP} decreases with hydration at low MWP. - ΔY_{PP} increases with hydration at high MWP. - Linewidth decreases with hydration.	117
Sulphonated-Eumelanin Oxidized sulphonated-Eumelanin	- CW - 9.3 GHz - FM: 100 kHz - MA: 0.025 mT - MWP: 0.03 and 10 mW - Solid-state (Pellets)	- Hydration (0 and 80% RH)	- EPR signal intensity is independent of hydration. - g-value independent on hydration. - ΔY_{PP} decreases with hydration at low MWP. - ΔY_{PP} increases with hydration at high MWP. - Linewidth is independent of hydration.	117
Dopa-Eumelanin	- CW - 9.871 GHz - MWP: Power saturation experiment (max. 144.5 mW) - 296 K - Solid-state (powders)	- Microwave Power (max. 144.5 mW)	- Signal increase with microwave power until saturation and then decreases.	118
Dopa-Eumelanin	- CW - 33.843 GHz - MWP: Power saturation experiment (max. 6.3 mW) - 296 K - Solid-state (powders)	- Microwave Power (max. 6.3 mW)	- Signal increase with microwave power until saturation and then decreases.	118
Dopa-Eumelanin	- Pulsed - 34 GHz - EDFS: $\pi/2 - \tau - \pi$ sequence ($\pi/2$ = 42 ns, π = 84 ns) - PFSR - Initial 296 K - Solid-state (powders)	- Temperature (20–110 K)	- T_1 relaxation time decreased with increasing temperature.	118
Black Soldier Fly (*Hermetia illucens*) Eumelanin	- CW[a] - 9 GHz - Solid-State and PBS Solution	- No specific variable	- Slight asymmetric signal.	119

FM: Field modulation; ΔY_{PP}: peak-to-peak height; MA: Modulation amplitude; MWP: microwave power; DMPO: 5,5-dimethyl-l-pyrroline-1-oxide; $\Delta H_{\frac{1}{2}}$: first-derivative peak' half-width at half-height of the positive-signal component; $P_{\frac{1}{2}}$: microwave power at which the saturation effect reduces the signal intensity by half; PBS: Phosphate-buffered saline; DMPO: 5,5'-dimethylpyrroline-1-oxide; EDFS: Echo detected field sweep; PFSR: Picket fence saturation recovery; CCR: carbon-centered radical; SFR: semiquinone free-radical; 4-MeO-PhN$_2$BF$_4$: 4-methoxybenzenediazonium tetrafluoroborate; RH: relative humidity. [a] Presumably, but not inferred in the paper.

concise overview of the prevailing EPR signal behavior corresponding to the commonly utilized external agents.

In light of the monomer-based perspective, the changes in the EPR signal can be attributed to a comproportionation equilibrium reaction, as depicted in Scheme 1. This reaction describes interactions between fully reduced and fully oxidized subunits forming an intermediate semi-reduced/semi-oxidized state.[82,90] External agents, some of which are listed in Table 2, can influence or alter this equilibrium by changing the forward (comproportionation) and reverse (disproportionation) reaction rate constants (k_C & k_D, respectively). In the case of eumelanin, the radical is the intermediate oxidative product. One way more radicals can be generated, or the reaction rates modified, is by increasing the pH as deprotonation shifts the equilibrium towards the product, or SQ radicals.[42,120]

Diamagnetic metal ions such as zinc (Zn^{2+}) and cadmium (Cd^{2+}) can also generate additional radicals. They can form

Scheme 1 The comproportionation equilibrium reaction. QH₂ and IQ species (top), resulting in the formation of SQ, an intermediate redox state, and protons (bottom). The opposite reaction is the disproportionation reaction. The preference between reactants and products will depend on the equilibrium between comproportionation (k_C) or disproportionation (k_D) reaction constants.

chelate complexes with the radicals, essentially removing them from the product "ledger" of the comproportionation reaction, leading to further SQ formation. In contrast, paramagnetic metal ions, such as copper (Cu^{2+}), iron (Fe^{3+}), or manganese (Mn^{2+}), can dramatically reduce eumelanin's radical EPR signal intensity.[80] The origin of the quench was not ascribed to a chemical reaction with eumelanin radicals but rather to the magnetic nature of the metal ions.[89] Indeed, it was observed consistent changes in amplitude (with no apparent differences in the linewidth) and microwave power saturation with the type and concentration of lanthanide ions with similar chemical properties but different magnetic properties, like Gadolinium (Gd^{3+}; paramagnetic) and Lanthanum (La^{3+}; diamagnetic). For instance, the addition of Gd^{3+} almost totally reduced the free-radical signal amplitude, whereas no significant signal alteration was obtained with La^{3+}.

Sarna *et al.* showed experimentally that Leigh's theory could be employed to explain the effect of transition metal ions on the radical signal mentioned above.[89] Leigh's approach considers magnetic dipoles fixed in space to a system composed of a metal ion in the vicinity of a radical. The interaction between the metal ion and the radical will induce a dipolar broadening of the narrow radical EPR signal, and the magnitude will depend on the ion's concentration. Additionally, the spin–lattice relaxation of the metal ion will modulate the interaction of the magnetic dipole by efficiently decreasing the dipolar broadening of the radical EPR signal.[89,120,121] Consequently, the higher the spin–lattice relaxation rate of the metal ion, the weaker the dipolar broadening; therefore, the smaller the decrease in the radical EPR signal intensity. In eumelanin's case, the Leigh-type effect decreases for metal ions with a short T_1, followed by an increase in the free-radical $P_{\frac{1}{2}}$. Except for Gd^{3+}, the lanthanide metals analyzed (and especially Dysprosium Dy^{3+} and Thulium Tm^{3+}) increased $P_{\frac{1}{2}}$ due to their high magnetic moments and $2\pi\upsilon T_1 \approx 1$. Nonetheless, it should be noted that a recent study on Cu-doped eumelanin shown that a chemical reaction with eumelanin radicals (eqn (12)) can also lead to a loss of signal.[22]
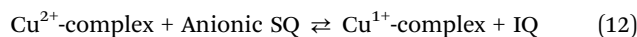
$$Cu^{2+}\text{-complex} + \text{Anionic SQ} \rightleftharpoons Cu^{1+}\text{-complex} + IQ \qquad (12)$$

Table 3 EPR signal features and changes commonly associated with eumelanin

Physicochemical agent	Spectral alteration
—	- Voight-like line shape with slight asymmetry - Homogeneous power saturation - Broader range of g-values for natural sourced eumelanin compared to synthetic derivative - g-values remained the same for poly-DHI and poly-DHICA. - Broader $\Delta H_{\frac{1}{2}}$ and higher spin concentration for poly-DHI compared to poly-DHICA.
Hydration	- Hydration-dependent spin concentration/signal intensity - g-value statistically independent on hydration. - ΔY_{PP} increases with hydration at high MWP - ΔY_{PP} decreases with hydration at low MWP (& acidic and neutral materials) - ΔY_{PP} is independent of hydration for alkaline samples - Linewidth decreases with hydration
Light irradiation	- Reversible increase signal amplitude - g-values increases - Lineshape increases - Signal amplitude increases - Enhancement of saturation characteristics - Radicals can be destroyed with continuous illumination - More effective at shorter wavelengths
Metal ions	- Type of ions influences signal amplitude and $P_{\frac{1}{2}}$ - Increase in linewidth - Reversible behavior
pH	- increasing pH: g-value increases, concentration increases, $\Delta H_{\frac{1}{2}}$ decreases, and line asymmetry gets more pronounced
Temperature	- Arrhenius behavior in solution - Curie–Weiss law behavior in solid-state and frozen solutions

(a) Eumelanin-copper complex by monodentate carboxyl binding

(b) Eumelanin-copper complex by bidentate nitrogen-carboxyl binding

pH < 7   pH > 7

(c) Eumelanin-copper complex by phenolic hydroxyl binding

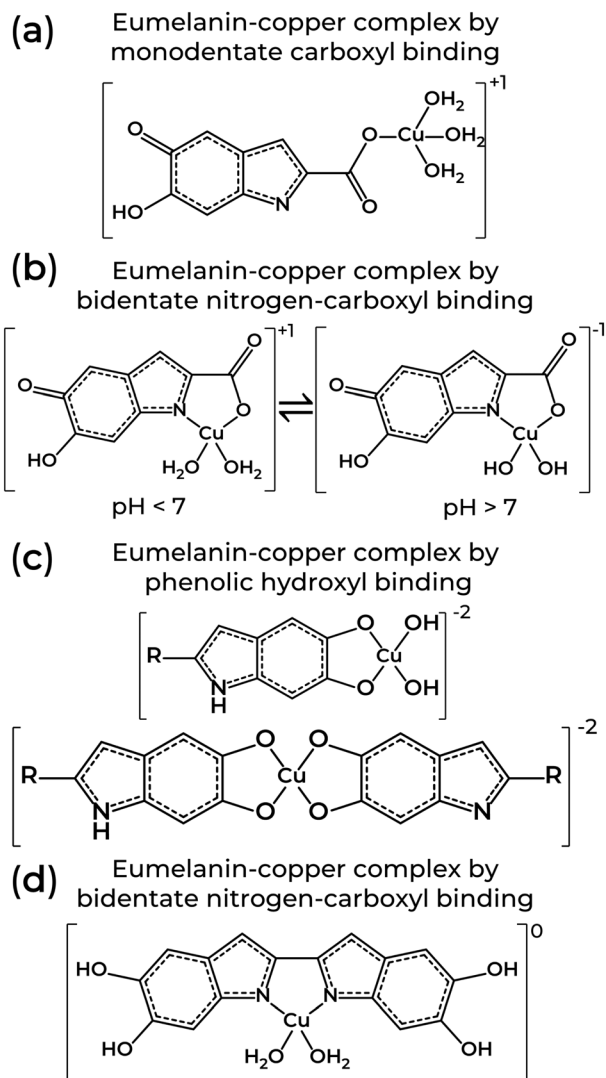### (d) Eumelanin-copper complex by bidentate nitrogen-carboxyl binding

Fig. 5 Structures of eumelanin-copper coordination involving one or two monomeric units from eumelanin through (a) monodentate carboxyl, (b) bidentate nitrogen-carboxyl, (c) phenolic hydroxyl, and (d) bidentate nitrogen-carboxyl binding. Structures adapted from T. Sarna *et al.* (1980)[122] and W. Froncisz *et al.* (1980).[85]

Eumelanin EPR spectra analysis was also used to determine the molecular nature of the binding sites on natural and synthetic models using $^{63}Cu^{2+}$ as a molecular probe. Depending on the system's pH, the several functional groups in eumelanin lead to different copper complexes.[85,120,122] At pH < 7, the binding of cupric ions in eumelanin is predominantly to monodentate carboxyl complexes and bidentate nitrogen-carboxyl groups in the synthetic models only (Fig. 5a and b). The corresponding EPR spectral parameters for the ions were $g_{\parallel}$ = 2.26–2.34, $A_{\parallel}$ = 460–560 MHz and $g_{\perp}$ = 2.066–2.076. At $7 \leq pH \leq 11$, the preferential binding site was to bidentate hydroxyl, but tri- or even tetradentate oxygen and nitrogen complexes can also happen (Fig. 5c and d). At these mild alkaline conditions, $g_{\parallel}$ = 2.24–2.26, $A_{\parallel}$ = 560–579 MHz, and $g_{\perp}$ = 2.054–2.064. Above pH 11, Cu^{2+}-eumelanin complexes with

multiple monomeric units could be obtained. The spectroscopic parameter would be $g_{\parallel}$ = 2.18, $A_{\parallel}$ = 610–620 MHz, and $g_{\perp}$ = 2.050.

When the eumelanin's molecular structure remains intact, the EPR signal does not quench entirely.[83,84,120,123] In fact, as seen in Fig. 4c, the radical concentration of natural and synthetic eumelanin reaches a plateau below a certain pH level. This feature has led to the idea that SQ may not be the only free-radical in eumelanin but rather two independent free-radical types: intrinsic and extrinsic paramagnetic centers. The extrinsic center would be an inducible eumelanin free-radical capable of reporting the redox state of its functional groups and the molecular nature of the monomer units on the macrostructure outer surface.[120] On the other hand, the intrinsic center would be related to the eumelanin core, representing its molecular state and integrity.[108,120] It has been speculated that the intrinsic centers would be trapped entities within the growing oligomers and aggregation of its particles (steps 1 & 2, Fig. 1c), where they would have low chemical reactivity due to the unapproachability of any reactive extraneous agents.[80,120] This has support from kinetic EPR studies that found an enhancement of redox activity at high pH levels *vs.* at lower pH.[98] The intrinsic and extrinsic paramagnetic centers were years later named carbon-centered radicals (CCR) and semiquinone-free radicals (SFR), respectively.[113] We should reinforce here that, although SFR center was defined as *extrinsic* in the past, it does not mean that SFR does not belong to eumelanin but rather just its position on the structure surface. Indeed, the formation of superoxide and hydrogen peroxide on the eumelanin surface being attributed to the intrinsic eumelanin radical,[91] the extrinsic terminology is strengthened as this reduction activity should exclusively take place at the eumelanin particle's surface. Recent infrared spectroscopy analysis supports this idea.[124] Note that some authors prefer the use of *intrinsic* and *extrinsic* for radicals that are present in the dark and those that are photo-generated.[110] Given that the SFR can be photo-generated,[115] we believe our use of these terms is more consistent.

Motivated by this context, systematic spectral simulation was carried out on different pH-dependent EPR signals.[78] The computational analysis in Fig. 6 indicates that more than one paramagnetic center should be present in the eumelanin system, with one having a strong pH dependence. The study showed that Lines 1 & 2 dominate the EPR signal at acidic and neutral states, whereas alkaline media is dominated by Line 3. As low pH is the experimental condition to probe the intrinsic free-radicals, such a behavior is compatible with the presence of the CCR and SFR centers mentioned above. This idea of multiple radicals is consistent with older observations of multiple radical reactive centers under photo-irradiated (pH 7.6) conditions, though no commentary was given as to these redox centers' g-values.[98]

The solid-state investigations revealed analogous characteristics to those observed in solution.[78,113–115] The prevailing presence of CCR radicals is evident at low microwave power, as illustrated in Fig. 7a (black line). However, an increase in

Fig. 6 Variation of Dopa-Eumelanin spin populations with pH obtained from X-band EPR spectrum simulation considering three different Voight lines. In (a) pH 1.6, and (b) pH 12.3. (c) The spin concentration estimation of the three-component fitting. Reproduced with permission from J.V. Paulin *et al.* (2019).[78] Copyright© 2019, American Chemical Society.

microwave power not only diminishes the signal intensity but also introduces a distinctive feature at high g-values (Fig. 7a, gold line).[115] This feature is an indicative of radicals with close g-values but differing spin–lattice relaxation times.[51,52,78,113–115,117] The additional feature is further enhanced by exposing

eumelanin to ammonia vapor,[115] suggesting an induced pH-dependent free-radical concentration. Such a behavior implies that CCR alone cannot be responsible for the solid-state EPR signal. To add on, owing to a consistent absence of water content variation, the temperature dependence of solid-state eumelanin's EPR signal follows a typical Curie–Weiss behavior (signal intensity $\propto T^{-1}$),[80,111] as opposed to the Arrhenius dependence observed for semiquinone in solution.[84]

Similarly to pH, hydration can also affect the EPR signal of solid-state eumelanin materials. Hydration is known to decrease linewidth and signal intensity, as shown in Fig. 7b and inferred from Fig. 7c. Assuming the three radical species model of Fig. 5, it is possible to infer what component does as pH changes (Fig. 7c). These changes could be associated with the radicals' interaction with the number of water molecules in their close surrounding.[117]

Although the molecular nature of SFR is most likely related to anionic SQ species, the CCR, on the other hand, is not that well understood as to its molecular origin. To bring light to this situation, modern density functional theory (DFT) calculations were performed to model distinct monomers and dimers of potential eumelanin moieties in their cationic, anionic, and radical structures.[77] In this study, two distinct groups were observed, one with a g value around 2.0030 and the other with g ranging between 2.0045 and 2.0050 (Fig. 8a). Moreover, SQ species, usually associated with SFR centers, were not the only structure with high g-values. IQ-anion and QI-anion species also showed g-values close to 2.0050. In contrast, CCR centers are associated with N_{def}^+, QH_2-anion, and QH_2-cation. Due to the broader linewidth of the EPR signal at low pH, the low hyperfine coupling of QH_2-cation in relation to SQR, was initially considered an improbable origin. Based on the alignment of the energy levels around the frontier orbitals of the eumelanin monomeric structures, the high LUMO (lowest unoccupied molecular orbital) levels imply that QH_2 cannot act as electron traps.[78] Hence, the formation of QH_2-anion would be hindered. Instead, it was proposed that QH_2 species would donate electrons to N_{def}^+ originating the paramagnetic species of the CCR center: N_{def}-neutral and QH_2-cation ($QH_2^0 + N_{def}^+ \rightarrow QH_2^+ + N_{def}^0$).[78] Note that the stabilization of free radicals through electron trapping at deep defect states has also been proposed using the Hückel theory for band structures.[125] The co-existence of these two systems would give origin to the CCR's broader spectral line features. Coincidentally, the formation of N_{def}^+ during synthesis[126,127] at the inner part of eumelanin's macro-structure would make this CCR system protect from reactive exogenous entities capable of affecting the k_C/k_D constant and, as a consequence, exhibit low reactivity.

There is a monomer entity that has not been thoroughly considered as a potential contribution to the CCR signal, which may have a connection to the SFR: a protonated semiquinone. The SFR, as depicted above, is almost always considered in an anionic form and not in its protonated form. Even though there is currently no computational EPR work produced on this monomer, considering that the experimental pK_a of a protonated DHI-semiquinone has been established to be 6.8,[128] one

Fig. 7 (a) Solid-State CW-EPR spectra of eumelanin under vacuum. Adapted from A.B. Mostert *et al.* (2018)[115] under Creative Commons Attribution-NonCommercial License 4.0 (CC BY-NC). (b) Normalized spin-density variation as a function of water percent adsorbed of eumelanin. Reprinted with permission from A.B. Mostert *et al.* (2013).[113] Copyright© 2013, American Chemical Society. (c) Estimation of each radical species concentration of eumelanin (NFMel-I) and eumelanin-inspired materials (NFMel-S and NFMel-6P) at dry (vacuum) and wet (80% RH) conditions. Reprinted with permission from J.V. Paulin *et al.* (2020).[117] Copyright© 2020, American Chemical Society.
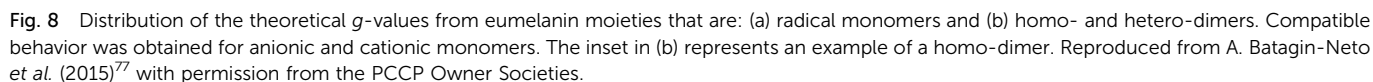
should anticipate that changes in the pH may lead to changes in the EPR signal around this value. This is consistent with the observations of Chio *et al.* (Fig. 4).[82] If careful attention is given to the literature, it is clear that a few authors have considered

the protonated moiety as a viable contributor to the EPR signal behavior.[82,84,99,129,130] In essence, if the semiquinone is protonated, the electron density's symmetry for the anionic form would be broken, which likely may lead to a concentration of the electron density on a carbon system, yielding a signal similar to a carbon-centered radical. If this is the case, the signal line width changes with pH can be neatly explained. However, what prevents us from ascribing CCR to a protonated semiquinone is the sheer persistence of the CCR. As established previously, the EPR signal in eumelanin is quite robust to several extreme conditions, such as high temperature and oxygenation, which does not comport with the easy manipulation of the semiquinone by "softer" variables such as hydration and moderate pH changes. As such, if the protonated semiquinone is present and is aligned with the CCR g-values, it may be that this signal *adds* to an additional internal or *intrinsic* radical, *e.g.*, those discussed previously as CCR candidates.

As eumelanin has an oligomeric macro-structure, a natural question would be whether one can use the spectral parameters of the monomeric units to evaluate the EPR spectrum of larger structures. Hence, DFT was applied to commonly reported dimers of two equal units (homo-structured dimers) or two different units (hetero-structured dimers). The data is depicted in Fig. 8b.[77] The g-values for homo-dimers remained consistent, with no discernible difference. In the hetero-dimers' case, the unprotected lateral oxygen units influence the spectroscopic features, following the IQ > QI > QH$_2$ order. This trend held true for most cases, except for the elevated g-values in SQ dimers in both scenarios. These results suggest that dimer or closely situated SQ species may not be entirely related to the SFR part of the EPR signal, which diverges from the prevailing consensus within the literature. This specific conclusion is consistent with what is known since the concentration of the induced radicals centers is relatively low, around one radical per 1000 monomer moieties,[85] making the probability of two SQ units in close neighboring also low. These computational studies may also form the future basis for understanding the differences between eumelanins that are DHI-rich *vs.* DHICA-rich, where their respective EPR spectra is modified, most likely due to different stacking morphologies.[38]

4. Multifrequency EPR and relaxation dynamics of eumelanin

High-frequency EPR spectroscopy has also been applied to eumelanin due to the higher spectral resolution avidable, which enables a better understanding of eumelanin's free-radical origin and molecular nature.[99,116,118,129,131] One of the first reports on Q-band EPR of a series of eumelanin and eumelanin-inspired materials was obtained by F.J. Grady and D.C. Borg back in 1968.[129] They showed that these materials had a broader asymmetrical spectrum in the Q-band with strong pH dependencies. These authors interpreted the asymmetry based on the presence of protonated radicals at lower pH and, at high pH, the formation of anionic radicals with high g-

Fig. 8 Distribution of the theoretical *g*-values from eumelanin moieties that are: (a) radical monomers and (b) homo- and hetero-dimers. Compatible behavior was obtained for anionic and cationic monomers. The inset in (b) represents an example of a homo-dimer. Reproduced from A. Batagin-Neto *et al.* (2015)[77] with permission from the PCCP Owner Societies.

value. The most important result from their work lies in the Q-band EPR spectrum of a simple 5-hydroxyindole-eumelanin (5-OH indole). The 5-OH indole EPR signal has a single broad line, which did not change with pH, that aligns with the low *g*-value components of the other natural and synthetic eumelanin (see Fig. 9a). Given that the formation of semiquinone would be difficult in such a system, the observed EPR signal makes plausible the presence of a paramagnetic species (potentially indole-like) protected from environmental variations, *i.e.*, the CCR or component thereof.

A few years later, a detailed computer simulations analysis on the EPR spectra recorded at Q-band (35 GHz) of frozen solutions of eumelanin at a wide range of pH was performed, Fig. 9b.[99] A combination of anionic *o*-SQ and cationic radicals was necessary for their analysis to simulate the EPR spectra adequately. At low pH, the unpaired electron of the protonated eumelanin would extend over several monomeric units. Nonetheless, with the increase of the pH, the eumelanin starts to deprotonate, converting the delocalized radical into the relatively localized SQ-anion. The authors also propose that a second ionization would originate another localized anion at
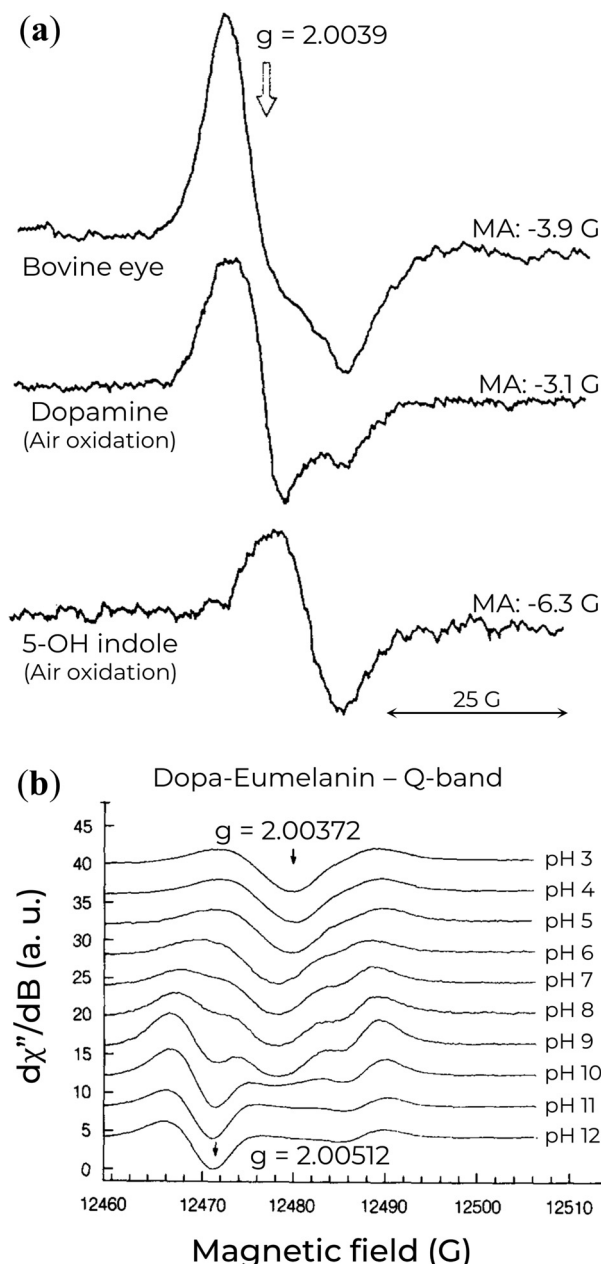
Fig. 9 (a) Q-band EPR spectra of eumelanin and eumelanin-inspired materials. *MA* indicates the modulation amplitude. Reprinted with permission from F.J. Grady and D.C. Borg (1968).[129] Copyright© 1968, American Chemical Society. (b) Variation of Q-band EPR signal of Dopa-Eumelanin as a function of pH. Reprinted with permission from M. Pasenkiewicz-Gierula and R.C. Sealy (1986).[99] Copyright© 1986, Elsevier B.V.

an extremely high pH. This species would be divided into two distinct radical groups. One of them would be pH-dependent and like anionic *o*-SQ ($g_\parallel$ = 2.0023 and $g_\perp$ = 2.0055), whereas the other would be associated with backbone defects and be pH-independent ($g_\parallel$ = 2.0023 and $g_\perp$ = 2.0038).[132]

The results obtained by Q-band EPR analysis are particularly gripping as they align with the current understanding of both CCR and SFR species, which have been extensively investigated

through spectral analysis and DFT calculations, as discussed in Section 3.

With the advances in EPR spectroscopy instrumentation, the examination and analysis of eumelanin materials have been measured at a very high frequency (263 GHz)[131] in the solid-state. The eumelanin high-resolution EPR spectra, shown in Fig. 10a, revealed two overlapping signals with relatively different *g*-anisotropies. One radical species is characterized by $g_x \approx$ 2.0042, $g_y \approx$ 2.0032, and $g_z \approx$ 2.0022, while the other is characterized by $g_x \approx$ 2.0037, $g_y \approx$ 2.0032, and $g_z \approx$ 2.0022.

DFT evaluation on the dependence of the *g*-tensor evaluated by the rhombicity $\left(\frac{g_x - g_y}{g_x - g_z}\right)$ as a function of *g*-anisotropy ($\Delta g = g_x - g_z$) of the different monomeric units in anionic, cationic, and neutral forms are summarized in Fig. 10b (colored squares, circles, and triangles).[131] Based on this plot, the two mentioned radicals can be ascribed to the previous species predicted (N_{def} and QH_2) by X-band EPR spectral analysis for CCR. The absence of SFR was explained by potential signal saturation or the neutral and solid-state nature of the samples, the two conditions known to increase the concentration of CCR.

To probe the intricate relaxation dynamics and electron-nuclear interactions in eumelanin (and eumelanin-inspired materials), advanced EPR techniques like electron-nuclear double resonance (ENDOR) have also been employed in a limited number of studies.[76,92,118,133,134] The implementation of this method has the potential to significantly contribute to enhancing the understanding of the molecular structure and dynamics of eumelanin radicals, as well as their spatial distribution and surrounding environment.[55]

The first result from ENDOR is the lack of a resolved structure or shoulders in the spectral wings (Fig. 10c), which indicates that eumelanin has a heterogeneity of trapping sites on its macrostructure, which is consistent with the widely accepted disorder model of eumelanin structure.[5,10]

The second result from the ENDOR technique shows that the relaxation time T_1 of eumelanin is greatly influenced by the radical and the local environment in which it exists.[76,92] Also, the degree of spatial uniformity of the radical distribution plays a significant role in determining T_2.[133] Notably, T_1 is consistent across different sources of eumelanin, and T_2 exhibits striking variation among them.[76,92,133]

In the solid state, the EPR signal of synthetic eumelanin quickly becomes saturated at low microwave powers and is demonstrated by very long relaxation time, T_1 = 4.3 ms and T_2 = 101 μs,[133] suggesting that the spins are decoupled from one another. These findings highlight the intricate interplay between radical type, local environment, and spatial uniformity in influencing the relaxation times of eumelanin, which could be further evidence of different spin populations found across various regions of the eumelanin's macrostructure. Indeed, when eumelanin was incubated in D_2O, there was observed minimal effect on its relaxation properties.[76] This behavior indicates that eumelanin has a free-radical (or at least one) well-protected or buried, compatible with CCR species.

Fig. 10 (a) 263 GHz EPR signal at different microwave powers and (b) Rhombicity as a function of g-value anisotropy of Dopa-Eumelanin. (a) and (b) Reprint from J.V. Paulin *et al.* (2021)[131] under Creative Commons Attribution-NonCommercial License 3.0 (CC BY-NC). (c) X-band EPR (top) and ENDOR (bottom) signal of natural eumelanin at 4.2 K with 3 mW of microwave power, 1.25 G of modulation amplitude, and −3 dB of RF power. Reprint with permission from T. Sarna *et al.* (1976).[76] Copyright© 1976, Elsevier Inc.

6. Future directions

The understanding of the eumelanin free-radical species is commonly investigated by X-band CW EPR. However, this methodology can exhibit certain limitations in providing comprehensive information on the electronic structure of these species. This limitation is being overcome using pH-dependent studies in multifrequency CW or pulsed EPR spectroscopy. Additionally, with the advance in magnetic resonance of the last decades, many advanced EPR techniques not yet explored in the eumelanin field could also be extremely important to understand the nature of each paramagnetic species and their dynamics. Therefore, future research could focus on implementing the proposed strategies outlined below to address these gaps.

(i) *EPR imaging*:[135–138] this technique exposes a sample placed in a magnetic field to electromagnetic radiation, allowing the paramagnetic species to emit radiation detected by a receiver coil. A two- or three-dimensional image of the sample will be constructed by obtaining the emitted radiation from various points. Although this method may not be useful to understanding the nature of the paramagnetic species of melanin and their dynamics, it could assist in investigating their distribution and concentration.

As we mentioned before, pulsed EPR can provide detailed information on the electronic and nuclear structure of paramagnetic species. It relies on the alignment of the electron spin magnetization in the presence of a constant field. This approach encompasses several techniques, each with unique characteristics,[55,67,139–142] that will be elaborated in the subsequent subsections.

(ii) *Electron-nuclear double resonance* (ENDOR) and *electron spin echo envelope modulation* (ESEEM): these techniques can probe the transitions involving nuclear spin flips driven by radiofrequency radiation and provide information on the electronic and nuclear spin interactions and the local structure of paramagnetic species. ENDOR often provides information on strongly coupled nuclei, whereas ESEEM detects more weakly coupled nuclei.

(iii) *Hyperfine-sublevel-correlation spectroscopy* (HYSCORE): it analyzes the hyperfine interactions between an unpaired electron and its neighboring nuclear spins. Besides determining the strength of the hyperfine interactions, obtaining information on the number, type, and position of the coupled nuclei is possible.

(iv) *Double electron–electron resonance* (DEER): this is a two-frequency technique capable of estimating the distance between two weakly-coupled electron spins based on the magnetic dipole–dipole. It elucidates distances, orientation, and conformational flexibility of specific structural features on the nanometer scale.

It is speculated that the paramagnetic species of eumelanin is a key feature that determines some of its physicochemical properties, for instance, charge transport,[40,42,114,143,144] photoconductivity,[145] and photodynamics.[115,146] Hence, other techniques that could be interesting to investigate are:

(v) *Optically Detected Magnetic Resonance* (ODMR):[147–151] it is a powerful spectroscopic technique capable of detecting the electron spin resonance transitions of paramagnetic species using optical techniques. The method involves optically exciting the sample and then monitoring the fluorescence,

phosphorescence, or absorption from the excited state as a function of an applied magnetic field over a wide range of temperature, pH, and excitation wavelength parameters. This methodology is commonly used for higher quantum efficiency materials, which is not the case for eumelanin.[152,153] However, spin-locking, pulse sequence, and cryogenic temperatures can be applied to improve the signal-to-noise ratio and obtain a stronger ODMR signal.

(vi) *Electrically detected magnetic resonance* (EDMR):[154–157] this magnetic resonance spectroscopy can provide information on free radicals' electronic and magnetic properties by measuring the spin-dependent transport of charge carriers under the influence of a magnetic field. Compared to conventional EPR, EDMR is extremely sensitive, down to 100 spins (at liquid helium temperatures).[158] The study of EDMR on eumelanin can be of high complexity due to the presence of multiple paramagnetic species and their environmental-dependent stability.

An additional avenue for future research may leverage recent advancements in engineering eumelanin's chemical structure. For example, the manipulation of the number of carboxylate (DHICA) and non-carboxylate (DHI) units, as well as the availability of different polymerization positions, packing arrangements, and macrostructures, along with covalent-bounded protection of co-existing redox-states[5,38,159] may facilitate the determination of the type and environment of the radicals. Accordingly, incorporating the methods mentioned in this review with controlled parameters of pH and temperature, along with a variety of eumelanin-related materials, can significantly enhance the comprehension of eumelanin's paramagnetic system.

To bring matters to a close, it's worth noting that some of the studies referenced here are rather dated. Performing a pH-dependent study, similar to the one conducted by Chio et al.[82] (Fig. 4), on solutions using a modern spectrometer with additional advanced modeling would be immensely useful, especially when coupled with power saturation and pulsed EPR techniques. Additionally, the choice of solvent in these experiments might play a crucial role in influencing the paramagnetic properties of eumelanin and should be carefully considered in future investigations. These cutting-edge approaches and considerations will undoubtedly contribute to a deeper understanding of the paramagnetic nature of eumelanin and its potential implications.

7. Conclusion

The central subclass of the melanin family of natural pigments known as eumelanin has unique physical and chemical properties. The strong and persistent paramagnetic signal is one of them, and it is not fully comprehended yet. This review summarizes the rich literature on eumelanin's multifrequency and time-dependent EPR characterization. Solution and solid-state results are showcased to discuss the potential origin of the paramagnetic signal. The in-depth analysis indicates a complex paramagnetic system for eumelanin. Indeed, the superposition of at least two different paramagnetic signals is expected to compose eumelanin's EPR spectrum.

Data availability statement

Data sharing does not apply to this article as no datasets were generated or analyzed during the current study.

Author contributions

J.V. Paulin: conceptualization, validation, investigation, writing – original draft, visualization. C.F.O. Graeff: conceptualization, validation, investigation, writing – review & editing. A.B. Mostert: conceptualization, validation, investigation, writing – review & editing.

Conflicts of interest

There are no conflicts to declare.

Acknowledgements

References

1 P. Meredith, C. J. Bettinger, M. Irimia-Vladu, A. B. Mostert and P. E. Schwenn, *Rep. Prog. Phys.*, 2013, **76**, 034501.
2 M. Irimia-Vladu, *Chem. Soc. Rev.*, 2014, **43**, 588–610.
3 M. Irimia-Vladu, Y. Kanbur, F. Camaioni, M. E. Coppola, C. Yumusak, C. V. Irimia, A. Vlad, A. Operamolla, G. M. Farinola, G. P. Suranna, N. González-Benitez, M. C. Molina, L. F. Bautista, H. Langhals, B. Stadlober, E. D. Głowacki and N. S. Sariciftci, *Chem. Mater.*, 2019, **31**, 6315–6346.
4 N. Amdursky, E. D. Głowacki and P. Meredith, *Adv. Mater.*, 2019, **31**, 1802221.
5 J. V. Paulin and C. F. O. Graeff, *J. Mater. Chem. C*, 2021, **9**, 14514–14531.
6 A. B. Mostert, *Polymers*, 2021, **13**, 1670.
7 J. V. Paulin and C. C. B. Bufon, *Submitted*.

8   M. D'Ischia, K. Wakamatsu, A. Napolitano, S. Briganti, J.-C. Garcia-Borron, D. Kovacs, P. Meredith, A. Pezzella, M. Picardo, T. Sarna, J. D. Simon and S. Ito, *Pigm. Cell Melanoma Res.*, 2013, **26**, 616–633.

9   M. D'Ischia, K. Wakamatsu, F. Cicoira, E. Di Mauro, J. C. Garcia-Borron, S. Commo, I. Galvàn, G. Ghanem, K. Koike, P. Meredith, A. Pezzella, C. Santato, T. Sarna, J. D. Simon, L. Zecca, F. A. Zucca, A. Napolitano and S. Ito, *Pigm. Cell Melanoma Res.*, 2015, **28**, 520–544.

10 M. d'Ischia, A. Napolitano, A. Pezzella, P. Meredith and M. J. Buehler, *Angew. Chem., Int. Ed.*, 2020, **59**, 11196–11205.

11 P. Meredith and T. Sarna, *Pigm. Cell Res.*, 2006, **19**, 572–594.

12 W. H. Koch and M. R. Chedekel, *Photochem. Photobiol.*, 1986, **44**, 703–710.

13 B. A. Gilchrest, M. S. Eller, A. C. Geller and M. Yaar, *N. Engl. J. Med.*, 1999, **340**, 1341–1348.

14 F. P. Noonan, M. R. Zaidi, A. Wolnicka-Glubisz, M. R. Anver, J. Bahn, A. Wielgus, J. Cadet, T. Douki, S. Mouret, M. A. Tucker, A. Popratiloff, G. Merlino and E. C. De Fabo, *Nat. Commun.*, 2012, **3**, 884.

15 D. M. A. Mann and P. O. Yates, *Mech. Ageing Dev.*, 1983, **21**, 193–203.

16 R. J. D'Amato, Z. P. Lipman and S. H. Snyder, *Science*, 1986, **231**, 987–989.

17 F. A. Zucca, G. Giaveri, M. Gallorini, A. Albertini, M. Toscani, G. Pezzoli, R. Lucius, H. Wilms, D. Sulzer, S. Ito, K. Wakamatsu and L. Zecca, *Pigm. Cell Res.*, 2004, **17**, 610–617.

18 H. Fedorow, F. Tribl, G. Halliday, M. Gerlach, P. Riederer and K. L. Double, *Prog. Neurobiol.*, 2005, **75**, 109–124.

19 S. Z. Berg and J. Berg, *Front. Immunol.*, 2023, **14**, 1–17.

20 M. G. Reyes, F. Faraldi, R. Rydman and C. C. Wang, *Neurol. Res.*, 2003, **25**, 179–182.

21 M. Sheliakina, A. B. Mostert and P. Meredith, *Mater. Horiz.*, 2018, **5**, 256–263.

22 A. B. Mostert, S. Rienecker, M. Sheliakina, P. Zierep, G. R. Hanson, J. R. Harmer, G. Schenk and P. Meredith, *J. Mater. Chem. B*, 2020, **8**, 8050–8060.

23 N. L. Nozella, J. V. M. Lima, R. F. de Oliveira and C. F. D. O. Graeff, *Mater. Adv.*, 2023, **4**, 4732–4743.

24 Y. J. Kim, W. Wu, S. Chun, J. F. Whitacre and C. J. Bettinger, *Proc. Natl. Acad. Sci. U. S. A.*, 2013, **110**, 20912–20917.

25 P. Kumar, E. Di Mauro, S. Zhang, A. Pezzella, F. Soavi, C. Santato and F. Cicoira, *J. Mater. Chem. C*, 2016, **4**, 9516–9525.

26 R. Xu, A. Gouda, M. F. Caso, F. Soavi and C. Santato, *ACS Omega*, 2019, **4**, 12244–12251.

27 J. V. Paulin, S. L. Fernandes and C. F. O. Graeff, *Electrochem*, 2021, **2**, 264–273.

28 M. Ambrico, P. F. Ambrico, T. Ligonzo, A. Cardone, S. R. Cicco, A. Lavizzera, V. Augelli and G. M. Farinola, *Appl. Phys. Lett.*, 2012, **100**, 253702.

29 A. Wahab, N. Gogurla, J. Y. Park and S. Kim, *Adv. Mater. Technol.*, 2022, **7**, 2101271.

30 H. J. Nam, J. Cha, S. H. Lee, W. J. Yoo and D. Y. Jung, *Chem. Commun.*, 2014, **50**, 1458–1461.

31 M. Piacenti-Silva, J. C. Fernandes, N. B. de Figueiredo, M. Congiu, M. Mulato and C. F. D. O. Graeff, *AIP Adv.*, 2014, **4**, 037120.

32 T. F. Wu, B. H. Wee and J. D. Hong, *Adv. Mater. Interfaces*, 2015, **2**, 1500203.

33 Z. Tehrani, S. P. Whelan, B. Mostert, J. V. Paulin, M. M. Ali, E. D. Ahmadi, C. F. O. Graeff, O. J. Guy and D. T. Gethin, *2D Mater.*, 2020, **7**, 024008.

34 S. P. Whelan, Z. Tehrani, M. Peacock, J. V. Paulin, O. Guy and D. Gethin, *J. Electroanal. Chem.*, 2022, **904**, 115868.

35 J. V. Paulin, L. G. S. Albano, D. H. S. Camargo, M. P. Pereira, B. A. Bregadiolli, C. F. O. Graeff and C. C. B. Bufon, *Appl. Mater. Today*, 2022, **28**, 101525.

36 S. N. Dezidério, C. A. Brunello, M. I. N. da Silva, M. A. Cotta and C. F. O. Graeff, *J. Non Cryst. Solids*, 2004, **338–340**, 634–638.

37 J. P. Bothma, J. de Boor, U. Divakar, P. E. Schwenn and P. Meredith, *Adv. Mater.*, 2008, **20**, 3539–3542.

38 L. Panzella, G. Gentile, G. D'Errico, N. F. Della Vecchia, M. E. Errico, A. Napolitano, C. Carfagna and M. D'Ischia, *Angew. Chem.*, 2013, **52**, 12684–12687.

39 M. Reali, P. Saini and C. Santato, *Mater. Adv.*, 2021, **2**, 15–31.

40 J. V. Paulin, M. P. Pereira, B. A. Bregadiolli, J. P. Cachaneski-Lopes, C. F. O. Graeff and C. C. B. Bufon, *J. Mater. Chem. C*, 2023, **11**, 6107–6118.

41 E. V. Gan, H. F. Haberman and I. A. Menon, *Arch. Biochem. Biophys.*, 1976, **173**, 666–672.

42 A. B. Mostert, *Chem. Phys.*, 2021, **546**, 111158.

43 F. G. Cánovas, F. García-Carmona, J. V. Sánchez, J. L. I. Pastor and J. A. L. Teruel, *J. Biol. Chem.*, 1982, **257**, 8738–8744.

44 J. Cheng, S. C. Moss and M. Eisner, *Pigm. Cell Res.*, 1994, **7**, 263–273.

45 K. B. Stark, J. M. Gallas, G. W. Zajac, J. T. Golab, S. Gidanian, T. McIntire and P. J. Farmer, *J. Phys. Chem. B*, 2005, **109**, 1970–1977.

46 A. A. R. Watt, J. P. Bothma and P. Meredith, *Soft Matter*, 2009, **5**, 3754–3760.

47 C.-T. Chen, V. Ball, J. J. A. Gracio, M. K. Singh, V. Toniazzo, D. Ruch and M. J. Buehler, *ACS Nano*, 2013, **7**, 1524–1532.

48 P. A. Abramov, O. I. Ivankov, A. B. Mostert and K. A. Motovilo, *Phys. Chem. Chem. Phys.*, 2023, **25**, 16212–16216.

49 A. Büngeler, B. Hämisch and O. I. Strube, *Int. J. Mol. Sci.*, 2017, **18**, 1901.

50 B. Commoner, J. Townsend and G. E. Pake, *Nature*, 1954, **174**, 689–691.

51 C. P. Poole, *Electron Spin Resonance: A Comprehensive Treatise on Experimental Techniques*, John Wiley & Sons, New York, 2nd edn, 1983.

52 J. A. Weil and J. R. Bolton, *Electron Paramagnetic Resonance: Elementary Theory and Practical Applications*, Wiley, New York, 2nd edn, 2007.

53 M. Brustolon, *Electron Paramagnetic Resonance: A Practitioner's Toolkit*, Wiley, 1st edn, 2009.

54 K. U. R. Naveed, L. Wang, H. Yu, R. S. Ullah, M. Haroon, S. Fahad, J. Li, T. Elshaarani, R. U. Khan and A. Nazir, *Polym. Chem.*, 2018, **9**, 3306–3335.

55 M. M. Roessler and E. Salvadori, *Chem. Soc. Rev.*, 2018, **47**, 2534–2553.

56 R. Bramley and S. J. Strach, *Chem. Rev.*, 1983, **83**, 49–82.

57 A. Abragam and M. H. L. Pryce, *Proc. R. Soc. A*, 1951, **205**, 135–153.

58 K. Möbius, W. Lubitz and A. Savitsky, *Prog. Nucl. Magn. Reson. Spectrosc.*, 2013, **75**, 1–49.

59 M. Bennati and T. F. Prisner, *Rep. Prog. Phys.*, 2005, **68**, 411–448.

60 B. Odom, D. Hanneke, B. D'urso and G. Gabrielse, *Phys. Rev. Lett.*, 2006, **97**, 030801.

61 C. Hägerhäll, S. Magnitsky, V. D. Sled, I. Schröder, R. P. Gunsalus, G. Cecchini and T. Ohnishi, *J. Biol. Chem.*, 1999, **274**, 26157–26164.

62 D. J. Hirsh and G. W. Brudvig, *Nat. Protoc.*, 2007, **2**, 1770–1781.

63 M. Brustolon, *Electron paramagnetic spectroscopy a practitioner's toolkit*, Wiley-VCH, Hoboken, NJ., 2009.

64 G. R. Eaton, S. S. Eaton, D. P. Barr and R. T. Weber, *Quantitative EPR*, Springer, Vienna, 1st edn, 2010, pp. 107–113.

65 K. Möbius and A. Savitsky, *High-Field EPR Spectroscopy on Proteins and their Model Systems*, Royal Society of Chemistry, 2008.

66 A. Schweiger and G. Jeschke, *Principles of Pulse Electron Paramagnetic Resonance*, Oxford University Press, 1st edn, 2001.

67 *EPR Spectroscopy: Fundamentals and Methods*, ed. D. Goldfarb and S. Stoll, John Wiley & Sons Ltd, 2018.

68 S. Stoll and A. Schweiger, *J. Magn. Reson.*, 2006, **178**, 42–55.

69 S. Stoll, EasySpin - EPR spectrum simulation, **https://www.easyspin.org/**.

70 D. R. Duling, *J. Magn. Reson B*, 1994, **104**, 105–110.

71 G. R. Hanson, K. E. Gates, C. J. Noble, M. Griffin, A. Mitchell and S. Benson, *J. Inorg. Biochem.*, 2004, **98**, 903–916.

72 C. Bengs and M. H. Levitt, *Magn. Reson. Chem.*, 2018, **56**, 374–414.

73 R. Sealy, J. Hyde, C. Felix, I. Menon and G. Prota, *Science*, 1982, **217**, 545–547.

74 P. M. Plonka, *Exp. Dermatol.*, 2009, **18**, 472–484.

75 R. Sealy, J. Hyde, C. Felix, I. Menon, G. Prota, H. Swartz, S. Persad and H. Haberman, *Proc. Natl. Acad. Sci. U. S. A.*, 1982, **79**, 2885–2889.

76 T. Sarna, C. Mailer, J. S. Hyde, H. M. Swartz and B. M. Hoffman, *Biophys J.*, 1976, **16**, 1165–1170.

77 A. Batagin-Neto, E. S. Bronze-Uhle and C. F. O. Graeff, *Phys. Chem. Chem. Phys.*, 2015, **17**, 7264–7274.

78 J. V. Paulin, A. Batagin-Neto and C. F. O. Graeff, *J. Phys. Chem. B*, 2019, **123**, 1248–1255.

79 A. Zadlo, G. Szewczyk, M. Sarna, T. G. Camenisch, J. W. Sidabras, S. Ito, K. Wakamatsu, F. Sagan, M. Mitoraj and T. Sarna, *Pigm. Cell Melanoma Res.*, 2019, **32**, 359–372.

80 M. S. Blois, A. B. Zahlan and J. E. Maling, *Biophys J.*, 1964, **4**, 471–490.

81 H. S. Mason, D. J. E. Ingram and B. Allen, *Arch. Biochem. Biophys.*, 1960, **86**, 225–230.

82 S. Chio, J. S. Hyde and R. C. Sealy, *Arch. Biochem. Biophys.*, 1982, **215**, 100–106.

83 R. C. Sealy, C. C. Felix, J. S. Hyde and H. M. Swartz, in *Free Radicals in Biology*, ed. W. A. Pryor, Academic Press, New York, 1980, pp. 209–259.

84 S. Chio, J. S. Hyde and R. C. Sealy, *Arch. Biochem. Biophys.*, 1980, **199**, 133–139.

85 W. Froncisz, T. Sarna and J. S. Hyde, *Arch. Biochem. Biophys.*, 1980, **202**, 289–303.

86 R. J. Sever, F. W. Cope and B. D. Polis, *Science*, 1962, **137**, 128–129.

87 F. W. Cope, R. J. Sever and B. D. Polis, *Arch. Biochem. Biophys.*, 1963, **100**, 171–177.

88 K. Stratton and M. A. Pathak, *Arch. Biochem. Biophys.*, 1968, **123**, 477–483.

89 T. Sarna, J. S. Hyde and H. M. Swartz, *Science*, 1976, **192**, 1132–1134.

90 C. C. Felix, J. S. Hyde, T. Sarna and R. C. Sealy, *J. Am. Chem. Soc.*, 1978, **100**, 3922–3926.

91 C. C. Felix, J. S. Hyde, T. Sarna and R. C. Sealy, *Biochem. Biophys. Res. Commun.*, 1978, **84**, 335–341.

92 T. Sarna and J. S. Hyde, *J. Chem. Phys.*, 1978, **69**, 1945–1948.

93 C. C. Felix, J. S. Hyde and R. C. Sealy, *Biochem. Biophys. Res. Commun.*, 1979, **88**, 456–461.

94 T. Sarna, A. Duleba, W. Korytowski and H. Swartz, *Arch. Biochem. Biophys.*, 1980, **200**, 140–148.

95 R. Arnaud, G. Perbet, A. Deflandre and G. Lang, *Photochem. Photobiol.*, 1983, **38**, 161–168.

96 T. Sarna and R. C. Sealy, *Arch. Biochem. Biophys.*, 1984, **232**, 574–578.

97 T. Sarna, I. A. Menon and R. C. Sealy, *Photochem. Photobiol.*, 1985, **42**, 529–532.

98 T. Sarna, W. Korytowski and R. C. Sealy, *Arch. Biochem. Biophys.*, 1985, **239**, 226–233.

99 M. Pasenkiewicz-Gierula and R. C. Sealy, *Biochim. Biophys. Acta*, 1986, **884**, 510–516.

100 W. Korytowski, B. Kalyanaraman, I. A. Menon, T. Sarna and R. C. Sealy, *BBA, Biochim. Biophys. Acta, Gen. Subj.*, 1986, **882**, 145–153.

101 M. S. Jahan, T. R. Drouin and R. M. Sayre, *Photochem. Photobiol.*, 1987, **45**, 543–546.

102 K. J. Reszka and C. F. Chignell, *J. Am. Chem. Soc.*, 1993, **115**, 7752–7760.

103 R. Dunford, E. J. Land, M. Rozanowska, T. Sarna and T. G. Truscott, *Free Radic. Biol. Med.*, 1995, **19**, 735–740.

104 K. Jimbow, K. Reszka, S. Schmitz, T. Salopek and P. Thomas, Distribution of eu- and pheomelanins in human skin and melanocytic tumors, and their photoprotective vs. phototoxic properties, in *Melanin: Its role in human photoprotection*, ed. L. Zeise, M. R. Chedekeland T. B. Fitzpatrick, Valdenmar Publishing Company, Overland Park, KS, 1995, pp. 155–175.

105 M. M. Jastrzebska, H. Isotalo, J. Paloheimo, H. Stubb and B. Pilawa, *J. Biomater. Sci. Polym.*, 1996, 7, 781–793.

106 P. Goncalves, C. A. Brunello and C. F. O. Graeff, *Mol. Cryst. Liq. Cryst.*, 2002, **374**, 39–44.

107 B. Szpoganicz, S. Gidanian, P. Kong and P. Farmer, *J. Inorg. Biochem.*, 2002, **89**, 45–53.

108 T. Sarna, J. M. Burke, W. Korytowski, M. Rozanowska, C. M. B. Skumatz, A. Zareba and M. Zareba, *Exp. Eye Res.*, 2003, **76**, 89–98.

109 E. Chodurek, B. Pilawa, A. Dzierzega-Lecznar, S. Kurkiewicz, L. Swiatkowska and T. Wilczok, *J. Anal. Appl. Pyrolysis*, 2003, **70**, 43–54.

110 B.-L. Seagle, K. A. Rezai, E. M. Gasyna, Y. Kobori, K. A. Rezaei and J. R. Norris, *J. Am. Chem. Soc.*, 2005, **127**, 11220–11221.

111 P. J. Gonçalves, O. B. Filho and C. F. O. Graeff, *J. Appl. Phys.*, 2006, **99**, 104701.

112 M. E. Cano, R. Castañeda-Priego, A. Gil-Villegas, M. A. Sosa, P. Schio, A. J. A. De Oliveira, F. Chen, O. Baffa and C. F. O. Graeff, *Photochem. Photobiol.*, 2008, **84**, 627–631.

113 A. B. Mostert, G. R. Hanson, T. Sarna, I. R. Gentle, B. J. Powell and P. Meredith, *J. Phys. Chem. B*, 2013, **117**, 4965–4972.

114 S. B. Rienecker, A. B. Mostert, G. Schenk, G. R. Hanson and P. Meredith, *J. Phys. Chem. B*, 2015, **119**, 14994–15000.

115 A. B. Mostert, S. B. Rienecker, C. Noble, G. R. Hanson and P. Meredith, *Sci. Adv.*, 2018, **4**, eaaq1293.

116 M. Al Khatib, M. Harir, J. Costa, M. C. Baratto, I. Schiavo, L. Trabalzini, S. Pollini, G. M. Rossolini, R. Basosi and R. Pogni, *Molecules*, 2018, **23**, 1916.

117 J. V. Paulin, A. Batagin-Neto, P. Meredith, C. F. O. Graeff and A. B. Mostert, *J. Phys. Chem. B*, 2020, **124**, 10365–10373.

118 M. Al Khatib, J. Costa, M. C. Baratto, R. Basosi and R. Pogni, *J. Phys. Chem. B*, 2020, **124**, 2110–2115.

119 U. D'amora, A. Soriente, A. Ronca, S. Scialla, M. Perrella, P. Manini, J. W. Phua, C. Ottenheim, R. Di Girolamo, A. Pezzella, M. G. Raucci and L. Ambrosio, *Biomedicines*, 2022, **10**, 2945.

120 T. Sarna and H. A. Swartz, in *The Pigmentary System: Physiology and Pathophysiology*, ed. J. J. Nordlund, R. E. Boissy, V. J. Hearing, R. A. King, W. S. Oetting and J. Ortonne, Blackwell Publishing, 2nd edn, 2006, pp. 191–212.

121 J. S. Leigh, *J. Chem. Phys.*, 1970, **52**, 2594–2608.

122 T. Sarna, W. Froncisz and J. S. Hyde, *Arch. Biochem. Biophys.*, 1980, **202**, 304–313.

123 T. Sarna, *J. Photochem. Photobiol., B*, 1992, **12**, 215–258.

124 Z. V. Bedran, S. S. Zhukov, P. A. Abramov, I. O. Tyurenkov, B. P. Gorshunov, A. B. Mostert and K. A. Motovilov, *Polymers*, 2021, **13**, 4403.

125 D. S. Galvão and M. J. Caldas, *J. Chem. Phys.*, 1988, **88**, 4088–4091.

126 H. S. Raper, *Physiol Rev.*, 1928, **8**, 245–282.

127 F. G. Cánovas, F. García-Carmona, J. V. Sánchez, J. L. I. Pastor and J. A. L. Teruel, *J. Biol. Chem.*, 1982, **257**, 8738–8744.

128 A. T. Al-Kazwini, P. O'Neill, G. E. Adams, R. B. Cundall, B. Jacquet, G. Lang and A. Junino, *J. Phys. Chem.*, 1990, **94**, 6666–6670.

129 F. J. Grady and D. C. Borg, *J. Am. Chem. Soc.*, 1968, **90**, 2949–2952.

130 T. Sarna and H. M. Swartz, in *Atmospheric Oxidation and Antioxidants*, ed. G. Scott, Elsevier, Amsterdam, 1993, pp. 129–169.

131 J. V. Paulin, A. Batagin-Neto, B. Naydenov, K. Lips and C. F. O. Graeff, *Mater. Adv.*, 2021, **2**, 6297–6305.

132 T. Sarna and P. M. Plonka, in *Biomedical EPR, Part A: Free Radicals, Metals, Medicine, and Physiology*, ed. S. S. Eaton, G. R. Eaton and L. J. Berliner, Springer, US, 1st edn, 2005, pp. 125–146.

133 M. Okazaki, K. Kuwata, Y. Miki, S. Shiga and T. Shiga, *Arch. Biochem. Biophys.*, 1985, **242**, 197–205.

134 K. Tadyszak, R. Mrówczyński and R. Carmieli, *J. Phys. Chem. B*, 2021, **125**, 841–849.

135 G. R. Eaton, S. S. Eaton and M. M. Maltempo, *Int. J. Radiat. Appl. Instrum., Part A*, 1989, **40**, 1227–1231.

136 H. Jang, S. Subramanian, N. Devasahayam, K. Saito, S. Matsumoto, M. C. Krishna and A. B. McMillan, *Magn. Reson. Med.*, 2013, **70**, 1173–1181.

137 S. Steinert, F. Ziem, L. T. Hall, A. Zappe, M. Schweikert, N. Götz, A. Aird, G. Balasubramanian, L. Hollenberg and J. Wrachtrup, *Nat. Commun.*, 2013, **4**, 1607.

138 R. Mrówczyński, L. E. Coy, B. Scheibe, T. Czechowski, M. Augustyniak-Jabłokow, S. Jurga and K. Tadyszak, *J. Phys. Chem. B*, 2015, **119**, 10341–10347.

139 D. M. Murphy and R. D. Farley, *Chem. Soc. Rev.*, 2006, **35**, 249–268.

140 J. Harmer, G. Mitrikas and A. Schweiger, in *High Resolution EPR: Applications to Metalloenzymes and Metals in Medicine*, ed. L. Berliner and G. Hanson, Springer, New York, NY, 2009, pp. 13–61.

141 M. J. N. Junk, *Assessing the Functional Structure of Molecular Transporters by EPR Spectroscopy*, Springer, Berlin, Heidelberg, 2012, pp. 7–52.

142 R. A. Stein, A. H. Beth and E. J. Hustedt, *Methods Enzymol.*, 2015, **563**, 531–567.

143 A. B. Mostert, B. J. Powell, I. R. Gentle and P. Meredith, *Appl. Phys. Lett.*, 2012, **100**, 093701.

144 J. Wünsche, Y. Deng, P. Kumar, E. Di Mauro, E. Josberger, J. Sayago, A. Pezzella, F. Soavi, F. Cicoira, M. Rolandi and C. Santato, *Chem. Mater.*, 2015, **27**, 436–442.

145 A. B. Mostert, B. J. Powell, F. L. Pratt, G. R. Hanson, T. Sarna, I. R. Gentle and P. Meredith, *Proc. Natl. Acad. Sci. U. S. A.*, 2012, **109**, 8943–8947.

146 A. Wang, A. R. Marino, E. M. Gasyna, T. Sarna and J. R. Norris, *J. Phys. Chem. B*, 2009, **113**, 10480–10482.

147 E. T. Harrigan and N. Hirota, *J. Am. Chem. Soc.*, 1975, **97**, 6647–6652.

148 J. J. Davies, *Contemp. Phys.*, 1976, **17**, 275–294.

149 A. H. Maki, in *Biological Magnetic Resonance*, ed. L. J. Berliner and J. Reuben, Springer, Boston, MA, 1984, pp. 187–294.

150 D. Carbonera, *Photosynth. Res.*, 2009, **102**, 403–414.

151 E. Goovaerts, *eMagRes*, 2017, **6**, 343–358.

152 P. Meredith and J. Riesz, *Photochem. Photobiol.*, 2004, **79**, 211–216.

153 J. V. Paulin, A. G. Veiga, Y. Garcia-Basabe, M. L. M. Rocco and C. F. Graeff, *Polym. Int.*, 2018, **67**, 550–556.

154 C. F. O. Graeff, C. A. Brunello and R. M. Faria, *Synth. Met.*, 1999, **101**, 805–806.

155 C. Boehme and K. Lips, *Phys. Rev. B. Condens. Matter. Mater. Phys.*, 2003, **68**, 245105.

156 K. Kato and Y. Teki, *Phys. Chem. Chem. Phys.*, 2021, **23**, 6361–6369.

157 K. J. Myers, P. M. Lenahan, J. P. Ashton and J. T. Ryan, *J. Appl. Phys.*, 2022, **132**, 115301.

158 D. R. McCamey, H. Huebl, M. S. Brandt, W. D. Hutchison, J. C. McCallum, R. G. Clark and A. R. Hamilton, *Appl. Phys. Lett.*, 2006, **89**, 182115.

159 X. Wang, L. Kinziabulatova, M. Bortoli, A. Manickoth, M. A. Barilla, H. Huang, L. Blancafort, B. Kohler and J. P. Lumb, *Nat. Chem.*, 2023, **15**, 787–793.